Volume 44
DOE/DP40200-140

LLE Review

Quarterly Report

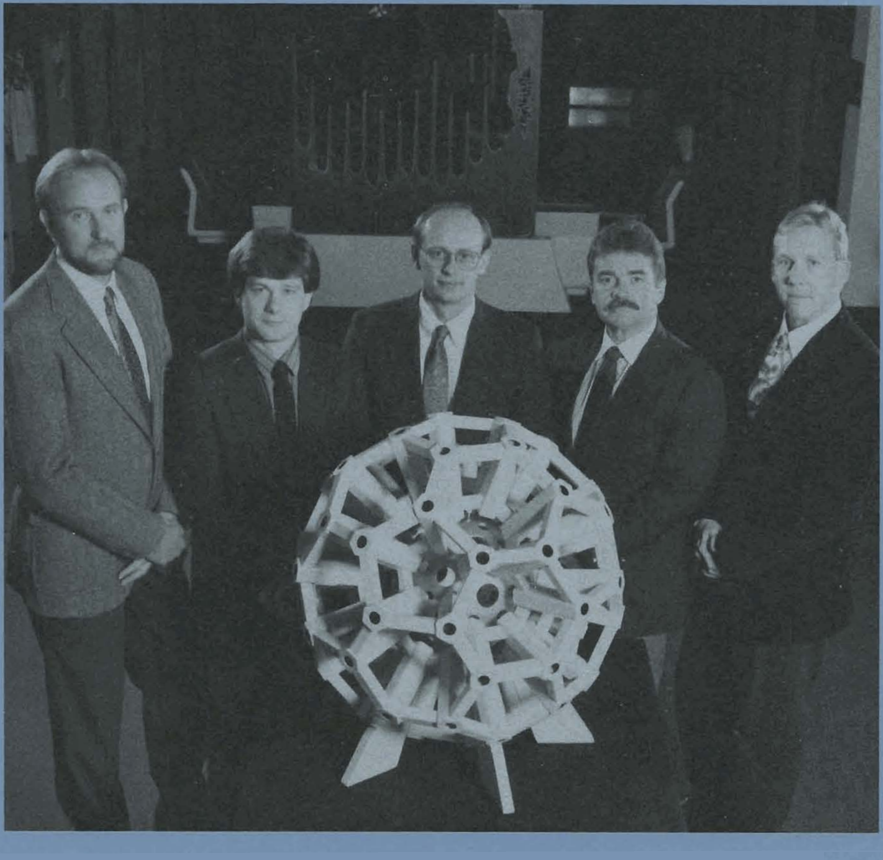

July–September 1990

Laboratory for Laser Energetics
College of Engineering and Applied Science
University of Rochester
250 East River Road
Rochester, New York 14623-1299

Volume 44
DOE/DP40200-140

LLE Review

Quarterly Report

Editor: S. A. Kumpan
(716) 275-7663

July–September 1990

Laboratory for Laser Energetics
College of Engineering and Applied Science
University of Rochester
250 East River Road
Rochester, New York 14623-1299

This report was prepared as an account of work conducted by the Laboratory for Laser Energetics and sponsored by Empire State Electric Energy Research Corporation, New York State Energy Research and Development Authority, Ontario Hydro, the University of Rochester, the U.S. Department of Energy, and other United States government agencies.

Results reported in the LLE Review should not be taken as necessarily final results as they represent active research. The views and opinions of authors expressed herein do not necessarily state or reflect those of any of the above sponsoring entities.

IN BRIEF

This volume of the LLE Review, covering the period July–September 1990, contains articles in two main sections: (1) the OMEGA Upgrade and (2) Advanced Technology Developments. The first article in Section 1 describes the changes in the overall system design of the 60-beam OMEGA Upgrade since the release of the OMEGA Upgrade Preliminary Design Document in October 1989. It is followed by an article that presents results of an investigation into stimulated rotational Raman scattering as it relates to the propagation of high-fluence ultraviolet laser beams in the OMEGA Upgrade. The third article is a report on the energy-transport measurements made on the multisegmented amplifier (MSA), built as a prototype amplifier for the original OMEGA Upgrade system configuration. The final article in Section 1 describes the design of the 20-cm-clear-aperture, single-segmented amplifier (SSA), which will be the final amplifier in the current OMEGA Upgrade system configuration. Section 2 presents the results to date of an intensive in-house effort at LLE to develop the various optical coatings required for the OMEGA Upgrade.

The highlights of this issue are

- The OMEGA Upgrade Preliminary Design Document (Title I document) set forth the design objectives and specifications for a laser system capable of delivering approximately 30 kJ of energy onto a fusion target, and presented a design that would meet them. Since that document was issued, the design of the OMEGA Upgrade has undergone several changes, primarily in the configuration of the beam-transport system. We present a description of the configuration changes and an update on the design concepts.

- Laser-fusion drivers, such as the OMEGA laser, require the propagation of many high-power laser beams over long paths in air to a target chamber. The threshold for certain nonlinear optical processes such as stimulated rotational Raman scattering (SRRS) in air depends on the product of the laser intensity times the air-interaction length. We present the results of preliminary experiments performed on OMEGA to determine the threshold intensity-length product for the generation of SRRS with various types of bandwidth, including smoothing by spectral dispersion (SSD).
- During the last quarter of 1989 final assembly and checkout were performed on the 24-cm-aperture MSA. The amplifier consists of two pairs of disk amplifiers, each five disks deep, that share a common central flash-lamp array. We report on the energy-transport measurements made on the MSA during the first and second quarters of 1990.
- The OMEGA Upgrade will use as its final amplifier a disk amplifier with a single 20-cm clear aperture. A prototype amplifier has been designed that incorporates the best aspects of existing disk-amplifier designs. In addition, the design emphasizes superior wave-front and polarization characteristics, gain over efficiency, and minimum maintenance over a lifetime in excess of 20,000 shots. This article describes that amplifier and its projected performance.
- The OMEGA Upgrade has dictated development of improved coating technologies at LLE. We report on coatings using standard evaporation methods and on those using an ion-assisted deposition (IAD) technique. Development of a sol-gel coating capability and related damage-test results are also reported for various substrates. Finally, development of an etching technique for distributed phase plates (DPP's) that can handle substantially higher fluences than previous designs is described.

CONTENTS

Page

IN BRIEF iii

CONTENTS v

Section 1 THE OMEGA UPGRADE 177
- 1.A OMEGA Upgrade System Design Update 177
- 1.B Stimulated Rotational Raman Scattering in Air 188
- 1.C Energy Transport Measurements in a Multisegmented Amplifier (MSA) 197
- 1.D Disk Amplifier Design for the OMEGA Upgrade 205

Section 2 ADVANCED TECHNOLOGY DEVELOPMENTS 219
- 2.A Development of Optical Coatings for the OMEGA Upgrade 219

Section 3 NATIONAL LASER USERS FACILITY NEWS 233

Section 4 LASER SYSTEM REPORT 234
- 4.A GDL Facility Report 234
- 4.B OMEGA Facility Report 235

PUBLICATIONS AND CONFERENCE PRESENTATIONS

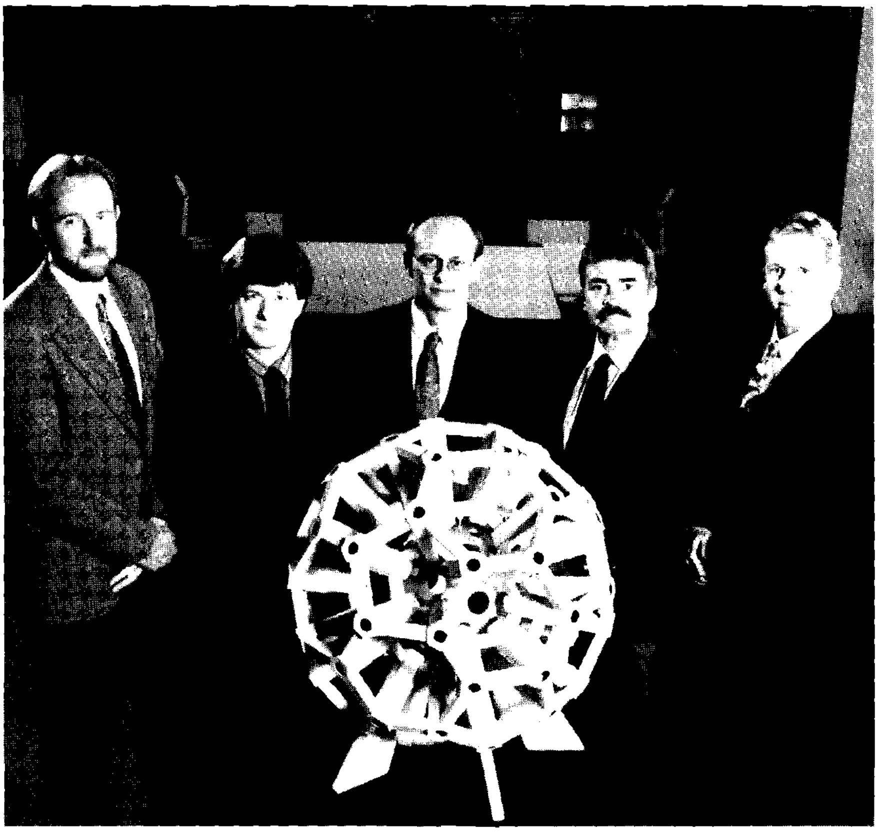

The OMEGA Upgrade Project will formally begin in FY91. The management team is shown standing behind a 1/12 scale model of the 60-beam, soccerball-shaped, target-mirror structure. From left to right they are: Dr. Thomas Boehly, Chief Engineer; Terrance Kessler, Requirements Review Board Chairperson; Steven A. Kumpan, Project Director; Robert Hutchison, Segment Manager for Beam Transport and Control Systems; and Samuel Morse, Segment Manager for Laser Systems.

Section 1
THE OMEGA UPGRADE

1.A OMEGA Upgrade System Design Update

The OMEGA Upgrade Preliminary Design Document (Title I document), which was submitted to DOE in October 1989, set forth the design objectives and specifications for a laser system capable of delivering approximately 30 kJ of energy onto a fusion target, and presented a design that would meet them.[1] Since that document was issued, the design of the OMEGA Upgrade has undergone several changes as a result of ongoing analysis. Some of the changes were necessary reconfigurations in the system layout while others were refinements of detailed design. The changes described herein have not altered the specifications to which the laser must perform, and these are summarized in Table 44.I.

The primary design change occurred in the configuration of the beam-transport system, which is all of the optical components between the frequency-conversion crystals and the target. This change was necessary to reduce the possibility of generating stimulated rotational Raman scattering (SRRS) in the high-powered 351-nm beams. The difference between the old and new beam-transport configurations is evident in the comparison of Fig. 44.1 and Fig. 44.2. In the new configuration the beams pass through the blue relays and straight into the target bay, eliminating the end and injection mirrors that were located in the laser bay. This raises the intensity threshold for SRRS in two ways: a reduction in the path length in air from the frequency-conversion crystals to target by the addition of blue relays, which provide a long vacuum path, and the reduction of beam fluence due to the 1.15X magnification of the relays. The stage C-D beam-splitting area was reconfigured in order to reduce the potential of mirror damage due to beam modulations induced by smoothing by spectral dispersion (SSD). This new system layout also allows room for the oscillators and driver lines in the laser bay. (The previous design placed these systems in the capacitor bay below the laser bay.) Additional changes that result from this reconfiguration will be outlined here as well.

Table 44.I: Performance goals of the OMEGA Upgrade system.

	Main Pulse		Foot Pulse	
Beam area (cm^2)	321		71	
Temporal shape	Gaussian		Half-Gaussian	
Crystal thickness L (cm)	0.76		1.6	
UV FWHM (ns)	0.50	0.75	3.0	5.0
IR FWHM (ns)	0.56	0.9	3.3	5.56
Nominal IR intensity on crystal I_0 ($\mathrm{GW/cm}^2$)	5.47	3.38	0.98	0.98
Normalized IR intensity of most intense ray(a)	5.14	3.18	4.08	4.08
Operating point of most intense ray(b)	M_1	M_2	F	F
Frequency-conversion efficiency (%)	80	70	75	75
IR energy-per-beam on to crystals (J)	977	977	116	194
UV energy-per-beam out of crystals (J)	782	684	87	146
UV energy-per-beam on target (J)(c)	564	493	62.7	105
Average UV energy loading after crystals ($\mathrm{J/cm}^2$)	2.4	2.1	1.2	2.1
AR damage fluence for full Gaussian ($\mathrm{J/cm}^2$)	3.8			6.8
Peak UV power on target (TW)	63.5	37.1	2.4	2.4
Total UV energy on target (kJ)	33.8	29.6	3.8	6.3
Truncated UV energy on target (kJ)(d)	27.1	23.7	3.8	6.3

(a) $0.9394\ I_0\ (L/0.76)^2$. See Fig. 39.3, LLE Review **39**, 120 (1989).

(b) See Fig. 39.3, LLE Review **39**, 120 (1989).

(c) Assumes a 9% transport loss and a DPP efficiency of 79% (into the central disk of the focal spot).

(d) With truncation of the last 20% of the main-pulse UV energy.

TC2631

Oscillator and Driver Lines

The redesign of the C and D split area has allowed room in the laser bay for the oscillators and driver lines. They have been moved from the capacitor bays beneath the laser bay up to the main laser-bay floor. The old and new configurations are depicted in Figs. 44.1 and 44.2.

The relocation of these components has reduced the path length between the driver lines and the A split area and has also reduced cost by decreasing the number of optics required.

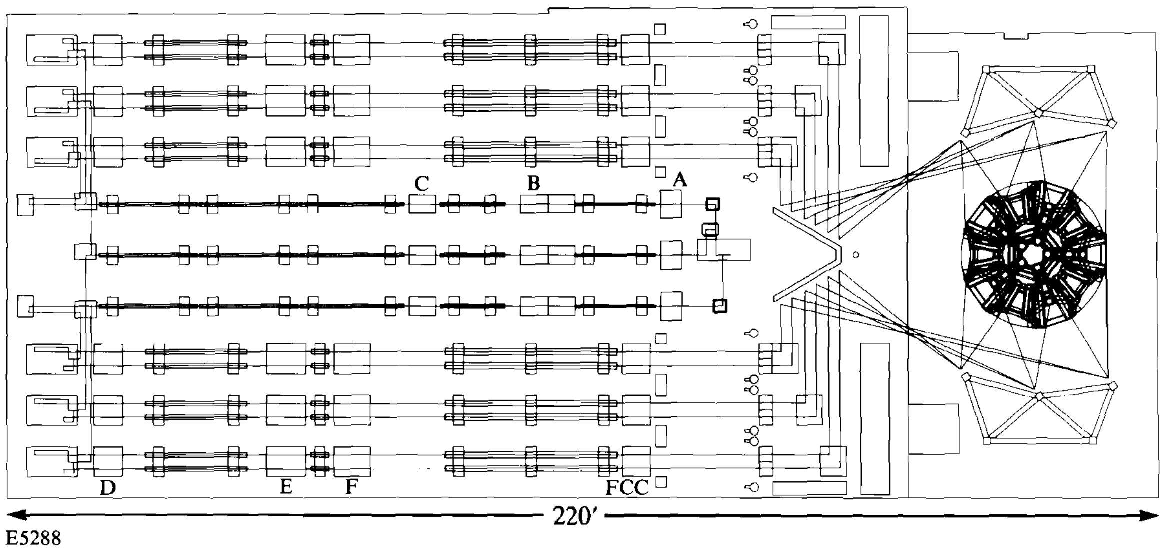

Fig. 44.1
Old OMEGA Upgrade layout.

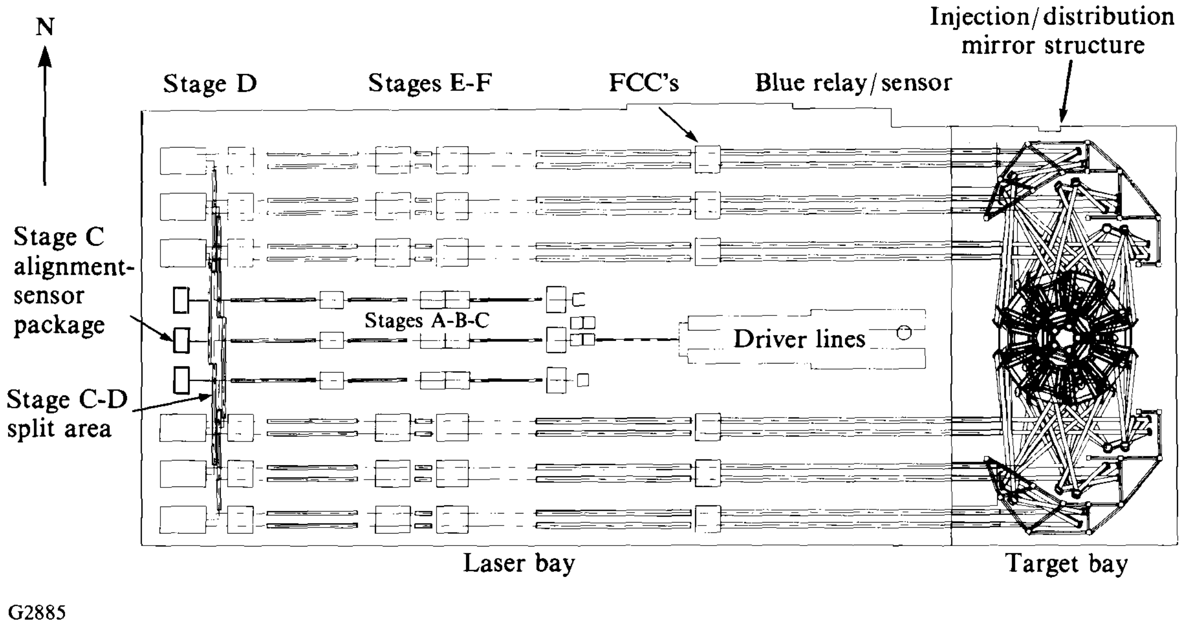

Fig. 44.2
New OMEGA Upgrade layout.

C and D Split Area

High-order spatial frequencies from diffraction and SSD modulation effects can cause nonuniformities in the beam (hot spots). If not controlled, the intensity of these hot spots, which increases with the distance from an image plane, can exceed the damage thresholds of the optical coatings used in the OMEGA Upgrade. To reduce the risk of damage from these modulation effects, a new C and D beam-splitting area has been designed that significantly reduces the path length from the relay output lenses to the image planes and eliminates 20 mirrors and their mounts from this portion of the laser system.

In the new design (see Fig. 44.2), just after the 64-mm stage-B amplifiers, three vertical groups of five beams are relayed to the stage-B spatial filters. These filters magnify each beam by 1.46, then relay them to the 90-mm stage-C amplifiers. After these amplifiers, the stage-C spatial filters relay the beam with no magnification to the stage-C output-mirror structures. At that point, 50% beam splitters divide each beam into two equal components, traveling either north or south and remaining arranged vertically (as shown in Fig. 44.3).

Half of the beams then encounter the stage-C end mirror, which has a 99.5% reflection coefficient. The 0.5% transmitted energy is used for the alignment-sensor package that will be a modified beam-diagnostic package from OMEGA. These alignment-sensor packages will perform alignment and energy measurements in stages A, B, and C. After the 50% beam splitters and the end mirrors, the 30 beams pass through the stage-C 1:1 relays, spatial-filter assemblies without pinholes.

At the output of the driver lines, images from driver-line gratings and apodizers are merged to form a single reference image. This primary image plane is propagated via the spatial filters and relays through the folding and splitting area. This final split divides the 30 beams into 60 beams. The beams are then directed to the stage-D amplifiers while maintaining nominally equal path lengths.

The new configuration requires that four clusters be elevated in order to maintain the shortest path length and to avoid having beams hitting mechanical components. To do this, vertical spacers were added to the appropriate support structures. The layout of the new C and D split area, as seen from floor level facing east, is shown in Fig. 44.4.

This new design has reduced the diffraction modulations at the output of the stage-C relays, and the SSD-induced modulation within the C and D split area has been cut in half. The cost benefit of the new configuration is the elimination of 20 mirrors along with their associated mounts and control systems.

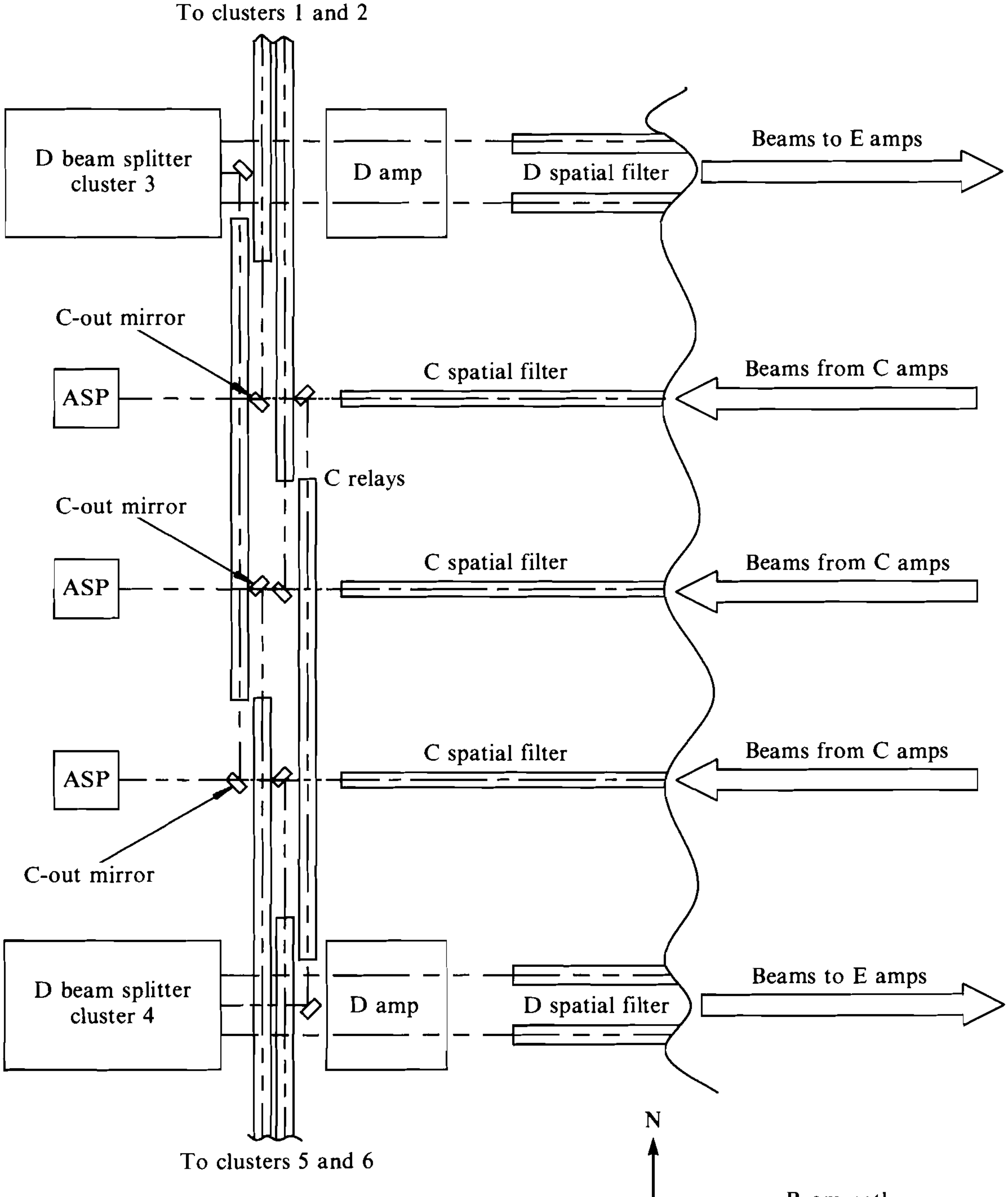

E5676

Fig. 44.3
Layout showing the direction of beam propagation and the location of the alignment-sensor packages (ASP's) after the C-mirrors.

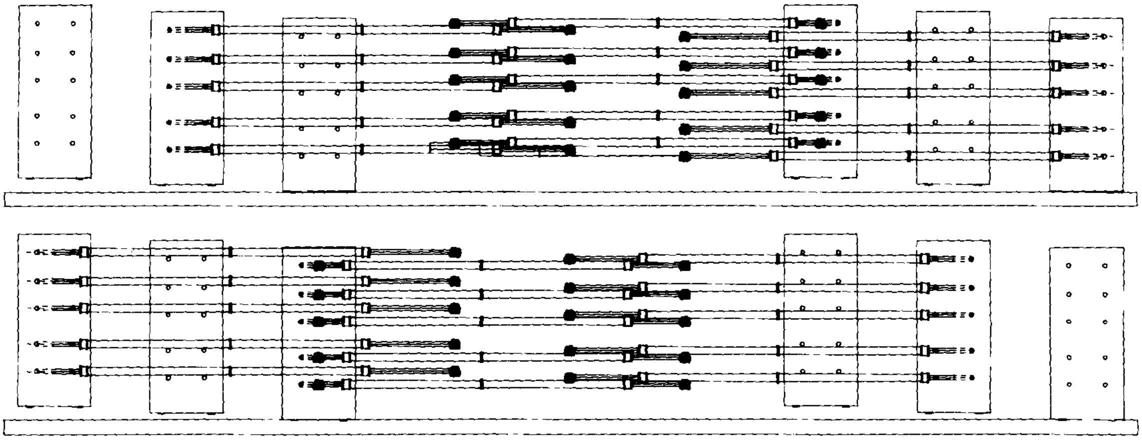

Fig. 44.4
Stage C and D split area as seen from the alignment-sensor packages (ASP's) looking toward the target bay.

Beam Transport and Blue Relays

The Title I system configuration shown in Fig. 44.1 has a beam-transport system that emulates the existing OMEGA beam transport and includes four mirrors per beam from the frequency-conversion crystals to the target-focus lenses. The configuration also incorporates all of the necessary alignment and diagnostic sensors in the laser bay. In the new configuration shown in Fig. 44.2, the end mirrors, which fold the beams to the injection mirrors in the center of the laser bay, were eliminated, thus the blue relays could be included in a straight-line configuration. This required a complete reconfiguration of the target-area mirrors, resulting in an injection and distribution mirror per beam in the target bay. The final target mirrors are located on the outside of the target-mirror structure as before. Inclusion of the blue relays also forced the creation of an alignment/diagnostic sensor subsystem that is integrated with the blue relays. An additional objective of the redesign exercise was to keep the number of large optical components per beam to a minimum.

In the original Title I design, the distance in air between the frequency-conversion crystals and the focus lenses was sufficient to possibly allow SRRS to cause an undesirable level of modulation of the beam. In addition, it is desirable to image the frequency-conversion crystals to the target mirrors to reduce the possibility of damage due to SSD modulations. The blue relays, which have a 17-m-long vacuum tube, will reduce SRRS in the UV beams propagated to the target chamber by reducing the total path length in air and by expanding the beam to reduce fluence. These relays transfer the image at the frequency-conversion crystals to a plane between the target mirrors and the focus lenses. In addition to image relaying, the blue relays also support beam alignment and diagnostic sensors. The blue-relay design concept is shown in Fig. 44.5.

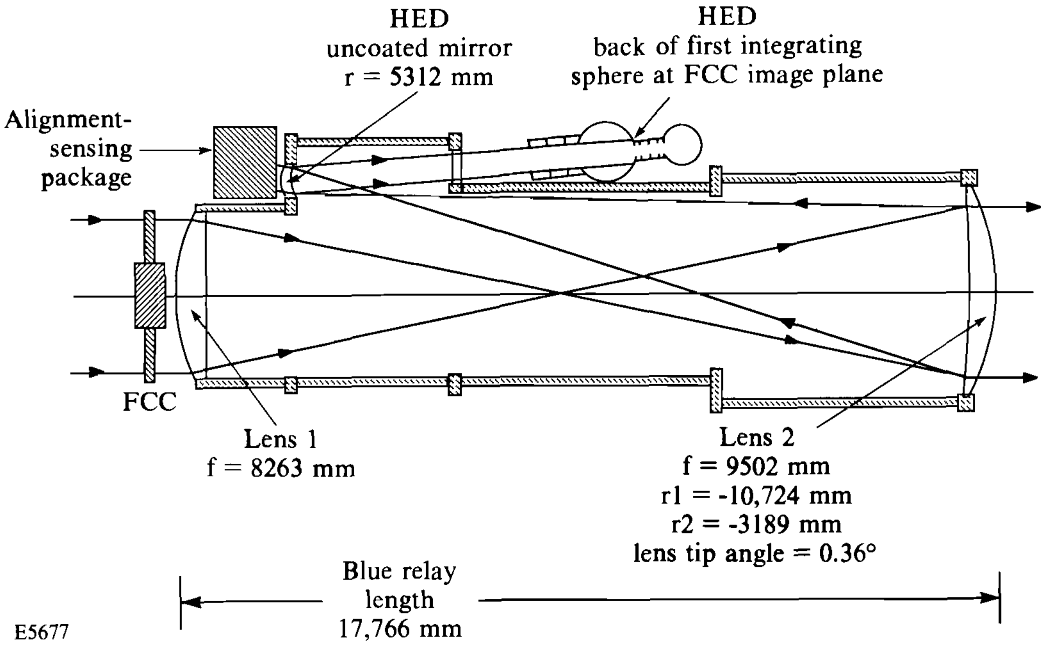

Fig. 44.5
Diagram of the blue image relays showing the integration of the alignment and harmonic-energy diagnostics.

The threshold for SRRS depends on the product of the beam intensity, the path length in air, and the bandwidth of the beam. The new configuration, which includes the blue relays, reduces the path length in air for the UV beam from 40 m to 23 m and expands the beam by a factor of 1.15 (thus reducing the beam intensity by 25%). These changes have raised the intensity threshold at which SRRS will occur to above the operating intensity of the upgraded OMEGA laser.[2,3]

Since the alignment and harmonic-energy diagnostics are incorporated in the blue-relay assemblies, it is not possible to use a pinhole to filter out the higher-order spatial frequencies. Furthermore, the unconverted red and green energy that is nearly focused at the pinhole plane would damage the pinhole and blow off unwanted debris in the vacuum. However, the improvement in the design due to the increase in the SRRS threshold and the elimination of 60 large mirrors far outweighs this drawback.

The alignment-sensor package on the blue relay will be used for beam pointing, centering, and pinhole alignment (at 1.054 μm) for stages D, E, and F. The blue alignment-sensor package is designed to be achromatic at 1.054 μm and 0.351 μm. Using two-dimensional image sensors, it will detect beam pointing and centering locations, and image processing will be done by the alignment computers. The accuracy will be ~1 μrad, as required for targeting.

The current concept for beam alignment from the frequency-conversion crystals to target uses a continuous-wave (cw), mode-locked, Q-switched, amplified laser, which is frequency tripled at the crystals to provide a UV beam for alignment. Computer-controlled rotating wave plates would be adjusted to send all of this energy down one or two of the beamlines. Auxiliary optics are required in the stage-F spatial filter to down-collimate the beam to achieve the necessary intensity for frequency conversion. Consistency in beam pointing would then be verified using the blue alignment-sensor package. An advantage of this technique would be the ability to check the angle tuning of the frequency-conversion crystals without performing full-system shots.

Once the laser beamlines are aligned in the IR, the UV-alignment beam is co-aligned with the red beam using the blue alignment-sensor package and transported to the target-mirror structure by the injection and distribution mirrors. The specific centering technique for this beam has yet to be determined, but image acquisition and processing will be used to determine its centering accuracy at the target mirror to within ±1 mm. Final target alignment can be accomplished by reflecting the beam off the target and back to auxiliary optics located in the focal plane of the blue relay, which then reflect the return beam into the blue alignment-sensor package. The auxiliary optics could consist of a polarizer, a quarter-wave plate, and a corner-cube reflector, as shown in Fig. 44.6.

Fig. 44.6
Alignment-sensing strategy showing the arrangement of the corner-cube assembly.

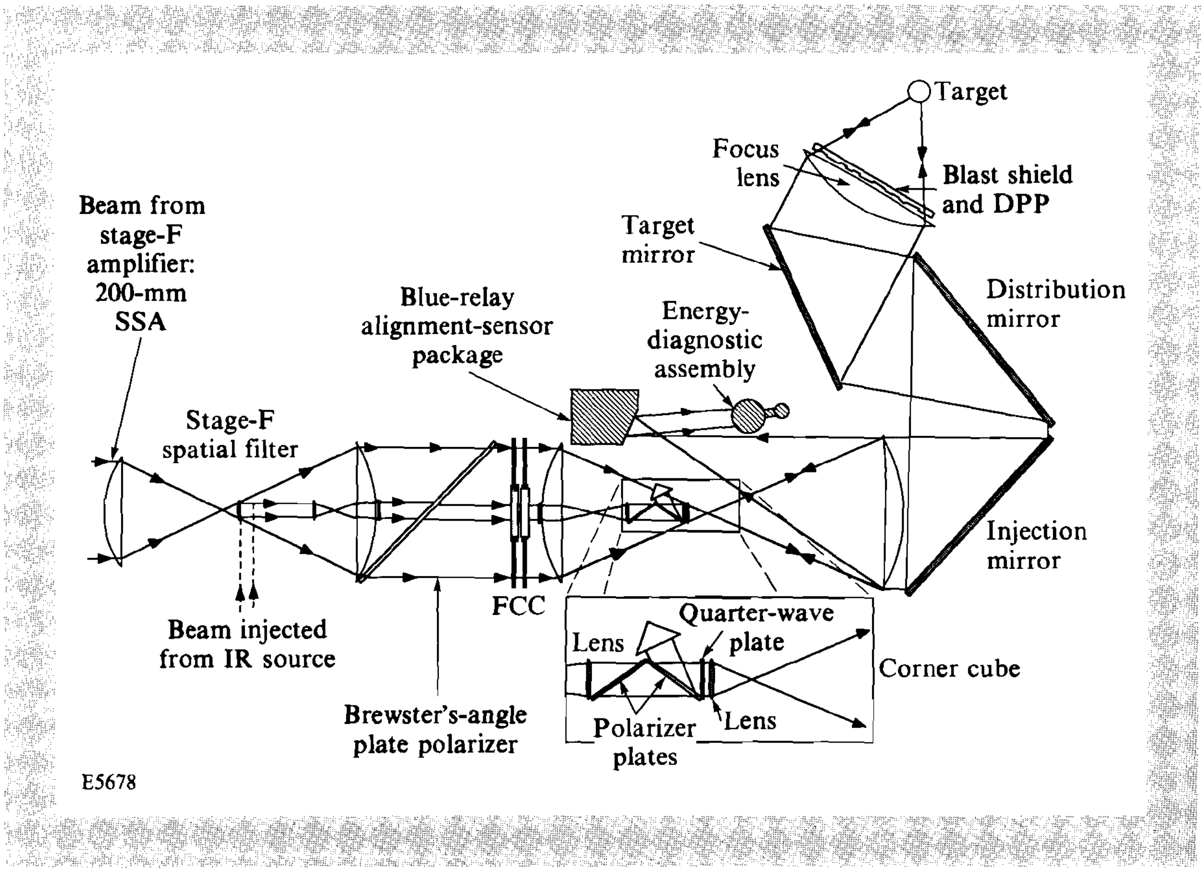

Harmonic-Energy Diagnostics

In order to monitor system performance, it will be necessary to separately measure the energy of the main and foot pulses in the co-propagated beam. The alignment-sensor packages, located after the stage-C end mirrors, will use calorimeters to separately measure the whole-beam IR energy in the foot and main pulses. Energy measurements made after the frequency-conversion crystals will be performed with the harmonic-energy diagnostics, a new version of the existing multiwavelength energy-sensing system[4] that utilizes two separate but coaxial integrating spheres, one each for the main and foot pulses. To meet the energy-balance specifications for the laser, the diagnostics must provide measurements of the UV energy on target that have an accuracy of 1%–2%. For power balance, the performance of the frequency-conversion crystals must also be monitored. To do this, the harmonic-energy diagnostics must measure the IR, green, and UV energies emerging from the crystals. A 4% reflection of the beam, from the first surface of the blue-relay output lens, will be injected into an integrating sphere containing four detectors with filters selected to measure each of three wavelengths: 0.351 μm, 0.527 μm, and 1.054 μm. At 0.351 μm, two detectors will supply redundant measurements.

The calibration of the harmonic-energy diagnostics will be accomplished using the SCI-Tech volume-absorbing calorimeters currently used as references in OMEGA. This technique involves tuning the frequency-conversion crystals to IR and using that beam-energy measurement as a baseline for successive measurements as the frequency-conversion crystals are tuned to green and UV.

Coatings

The laser system contains a large number of optics that require various types of coatings on one or more surfaces. Ongoing work in the Thin Film Technologies Group has demonstrated the ability to deposit coatings on small optics with damage thresholds satisfying the requirements of the laser system.[5] Viable designs have also been conceived for the transport optics and distributed phase plates. The article in Section 2 of this issue provides an in-depth report on the advances in those technologies.

Power Conditioning

The new power-conditioning system will provide significantly improved control of individual amplifiers than that currently used on OMEGA. While employing new approaches and designs, much of the existing OMEGA hardware will be reused. Each power-conditioning unit will have its own charging supply to facilitate individual control of the charge voltage. Instructions will be relayed from a single-host computer, via a three-conductor fiber-optic network, to a micro-controller located in each power-conditioning unit. The fiber-optic network has three lines: a communications line, an interlock line (the Ready Line), and a fire-synchronization-signal line. The power-conditioning units will be organized as eight groups connected in individual loops to serial ports on the host computer. One loop will control the driver lines, the second will control the stages-A–C amplifiers, and the other six will each control a single cluster of the stages-D–F amplifiers. Each micro-controller will be able to monitor interlock and status signals and relay that information back to the host computer.

In addition to building new rod power-conditioning units, existing OMEGA rod units will be modified to incorporate individual chargers and micro-controllers. For the single-segmented amplifiers, the design will be similar except that pre-ionization lamp-check circuits will be added. The specification for the single-segmented amplifier pulse-forming networks (PFN) are shown in Table 44.II.

Table 44.II: Specifications for the single-segmented amplifier (SSA), pulse-forming networks (PFN's).

		15-cm Amplifier	20-cm Amplifier
Linear resistance	(mΩ)	120	120
Pulse width	(μs)	550	550
Inductance	(μH)	160	160
Capacitance	(mF)	210	210
Charge voltage	(V)	14,162	14,102
Stored energy			
PFN	(J)	21,059	20,881
head	(J)	252,708	334,096

E5684

Control Systems

The OMEGA Upgrade will require over 2000 control channels for devices such as mirrors, positioners, shutters, etc. There are three main groups of devices to be controlled: two-state devices such as shutters and flip-ins; single-motor devices such as rotating wave plates; and dual-motor devices such as pinhole manipulators and mirror positioners. The current OMEGA alignment system is based on a computer-automated measurement and control (CAMAC) interface that employs multiplexed stepper-motor drivers to control the analog devices and digital input/output (I/O) devices to control the two-state devices. With ten times more devices to control, this approach becomes impractical due to the cost of cable installation and maintenance alone.

Several alternative approaches have been considered in terms of function and expense. The three most viable systems are a distributed CAMAC system, a distributed VERSAbus Motorola European (VME) system, and a serial network consisting of custom intelligent local device controllers.

An analysis of these systems shows that the serial network has significant cost advantages over the other two configurations; the primary savings are from the substitution of dc motors for stepper motors and the reduction of cabling requirements.

The serial network would be the backbone for a number of small, strategically positioned networks in the laser and target bays. Each intelligent controller would be linked to the network by low-cost coaxial cable, which is also simple to install. Each major device type will have a controller that employs a standard communications protocol being developed at LLE. A proposed layout is shown in Fig. 44.7.

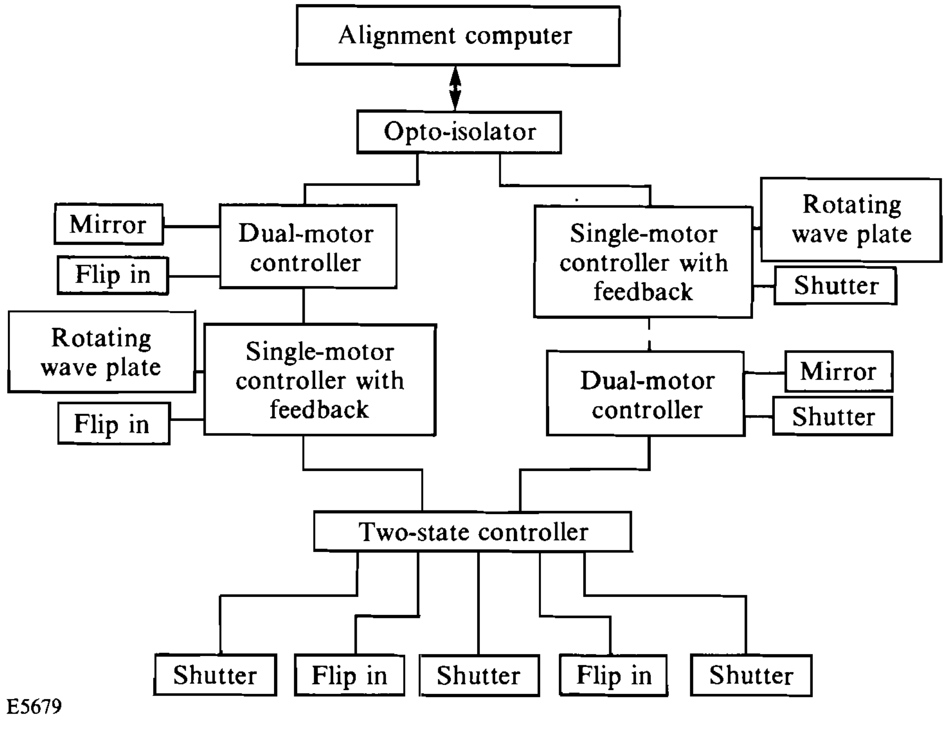

Fig. 44.7
Functional diagram of the control-system strategy using a serial loop.

In contrast to the systems currently in use, the new controllers will continuously monitor, report, and adjust the state of the device each controls. A clear advantage is simplicity since any anomalous behavior of the device is handled by the local controller without intervention of the host computer, which is ultimately notified via the serial network. This will greatly improve the response time to these events and relieve the host computer of most of the control processing. The serial nature of the network lends itself to easy expansion; adding a device is simply a matter of connecting the new device to the network and adding a subroutine to the host control program.

Summary

The new design was necessary to minimize the effects of SRRS on the uniformity of the beam. This was accomplished primarily by reconfiguration of the beam-transport mirrors and the addition of the blue relays, which facilitated the mounting of the energy and alignment diagnostics. The relocation of the oscillators and driver lines has made for a more compact configuration that is less costly and easier to operate and align. The refinements to the harmonic-energy diagnostics, power conditioning, and control-system designs are cost-effective solutions to some of the problems inherent to the original design. Completion of these new designs has provided a basis upon which better cost estimates and scheduling can be made. Our efforts will now concentrate on refining these designs and ultimately subjecting them to a final design review, expected to take place about one year after Upgrade Project funds are released to LLE.

ACKNOWLEDGMENT

This work was supported by the U.S. Department of Energy Division of Inertial Fusion under agreement No. DE-FC03-85DP40200.

REFERENCES

1. OMEGA Upgrade Preliminary Design Document, DOE/DP40200-101, Sec 2.3 (1989).
2. LLE Review **44**, 188 (1990).
3. M. Skeldon and R. Bahr, to be published in *Optics Letters*.
4. LLE Review **18**, 56 (1984).
5. LLE Review **44**, 219 (1990).

1.B Stimulated Rotational Raman Scattering in Air

Laser-fusion drivers, such as the OMEGA laser, require the propagation of many high-power laser beams over long paths in air to a target chamber. The threshold for certain nonlinear optical processes such as stimulated rotational Raman scattering (SRRS) in air[1-4] depends on the product of the laser intensity times the air-interaction length. Due to the high laser intensity-length products envisioned for the ultraviolet beams of the OMEGA Upgrade, the possibility of generating forward SRRS in air is of utmost concern. Moreover, schemes such as smoothing by spectral dispersion (SSD)[5] used to smooth the intensity distribution on target require the use of large optical bandwidths. The effects of certain bandwidths on the stimulated scattering process have been discussed by others; however, the effects of SSD on the SRRS process have only recently been investigated.[6] Preliminary experiments have been performed on OMEGA to determine the threshold intensity-length product for the generation of SRRS with various types of bandwidth, including SSD.

Theory

The scattering of light has been studied extensively over the last 100 years. Spontaneous light scattering occurs when optical radiation travels through a medium and is scattered by fluctuations in the refractive index brought about by random local material excitations within the medium. With the invention of the laser, a new type of scattering phenomena known as stimulated scattering was discovered. In stimulated scattering the spontaneously scattered radiation field can be strong enough to beat with the incident field and coherently drive the material excitation. Stimulated scattering occurs in high-intensity light beams of small divergence, and the spectrum of scattered light is significantly narrowed.

SRRS in air is a nonlinear process where the material excitation involves transitions between the molecular rotational levels of the molecules in the air. Since air is 80% nitrogen, the problem is approximated by scattering from N_2 molecules. The process can be modeled by including a nonlinear polarization term P^{NL} in the optical wave equation to account for the response of the medium to the optical fields present in the medium.[7] The optical wave equation for the total electric field E (i.e., the sum of the laser and scattered fields) in the medium is given by

$$\nabla^2 E(r,t) - \frac{n^2}{c^2}\frac{\partial^2}{\partial t^2}E(r,t) = \frac{4\pi}{c^2}\frac{\partial^2}{\partial t^2}P^{NL}(r,t), \qquad (1)$$

where c is the speed of light in vacuum, and n is the refractive index, assumed here to be independent of frequency.

To determine the material equation that describes the response of the medium to the optical fields, we write the energy U of the interaction between the polarizability α of an N_2 molecule and the local electric field E as

$$U = -\frac{1}{2}\sum_{ij}\alpha_{ij}E_iE_j. \qquad (2)$$

The force F (torque) driving the rotational oscillation is then given by

$$F = -\sum_k \frac{\partial U}{\partial Q_k} = \frac{1}{2}\sum_{ijk}\left(\frac{\partial \alpha_{ij}}{\partial Q_k}\right)E_iE_j, \qquad (3)$$

where Q is the rotational coordinate of the molecule. The collection of these localized rotational oscillations gives rise to a propagating optical phonon wave in the medium. We assume that the rotational oscillations are harmonic, giving the equation of motion for the rotational coordinate Q as

$$\mu\frac{\partial^2 Q_k}{\partial t^2} + \mu\Gamma\frac{\partial Q_k}{\partial t} + \mu\omega_R^2 Q_k = \frac{1}{2}\sum_{ij}\left(\frac{\partial \alpha_{ij}}{\partial Q_k}\right)E_iE_j, \qquad (4)$$

where ω_R is the resonance frequency of the rotational oscillation, μ is the reduced mass of the system, and the right-hand side of this equation is the force (torque) driving the rotational oscillations. In this equation, a damping term (second term on the left) has been added phenomenologically where Γ is the damping constant or linewidth for the Raman process. The nonlinear polarization in Eq. (1) can be obtained by expanding the electronic polarizability α of the medium in a Taylor series in one of its rotational coordinates and writing the i^{th} component of the polarization P_i of the medium in the form

$$P_i = \sum_j N\left(\alpha_{ij}\right)_0 E_j + \sum_{jk} N\left(\frac{\partial \alpha_{ij}}{\partial Q_k}\right) Q_k E_j + \ldots, \tag{5}$$

where N is the number of molecules taking part in the interaction. The nonlinear polarization of the medium in Eq. (1) can be approximated by the second term on the right in the above equation. (The first term is the linear term giving rise to the ordinary index of refraction of the medium.) The equation of motion for the optical phonon wave [Eq. (4)] along with the optical wave equation [Eq. (1)], form a set of coupled nonlinear differential equations for the optical fields and molecular rotations. When appropriate boundary conditions are applied, these equations describe the stimulated rotational Raman process in detail.

To solve the above equations we assume that the laser and Stokes fields (for simplicity, we assume only one Stokes field is present) can be represented by plane-wave expansions with slowly varying amplitudes [i.e., $E_i = 1/2\, A_i \exp(ik_i z - i\omega_i t) + cc$, with $i = L$ for the laser field and $i = S$ for the Stokes field] and similarly for the material wave [i.e., $Q = 1/2\, \tilde{Q} \exp(ik_R z - i\omega_R t) + cc$]. If we substitute these into the above equations and keep only those terms that are properly phase matched, we obtain the set of coupled wave-amplitude equations

$$\frac{\partial}{\partial z} A_L(z,t) + \frac{1}{v_L}\frac{\partial}{\partial t} A_L(z,t) = \frac{i\pi N\omega_L}{nc}\left(\frac{\partial \alpha}{\partial \tilde{Q}}\right) \tilde{Q}(z,t) A_S(z,t) \tag{6a}$$

$$\frac{\partial}{\partial z} A_S(z,t) + \frac{1}{v_S}\frac{\partial}{\partial t} A_S(z,t) = \frac{i\pi N\omega_S}{nc}\left(\frac{\partial \alpha}{\partial \tilde{Q}}\right) \tilde{Q}^*(z,t) A_L(z,t) \tag{6b}$$

$$\frac{\partial}{\partial t}\tilde{Q}(z,t) + \frac{\Gamma}{2}\tilde{Q}(z,t) = \frac{i}{4\mu\omega_R}\left(\frac{\partial \alpha}{\partial \tilde{Q}}\right) A_L(z,t) A_S^*(z,t). \tag{6c}$$

In deriving these equations we have assumed conservation of energy ($\omega_L - \omega_S = \omega_R$) and the phase-matching condition $k_L - k_S = k_R$. It can be seen from Eq. (6c) that the material response $\tilde{Q}$ is driven by the beating of the laser and Stokes fields.

The above coupled wave-amplitude equations can be solved if we assume that the laser field is nondepleted. The steady-state solution (neglecting time derivatives) for the Stokes intensity can be calculated by neglecting the first equation above and assuming the laser field to be constant in the second and third equations. The result gives

$$I_S(L) = I_S(0)\exp\left(gI_L L\right), \tag{7}$$

where we have used the definition of the intensity for wave i

$$I_i = ncA_i A_i^* / 8\pi,$$

$I_S(0)$ is the noise field to be amplified by the nonlinear process, L is the interaction length, and

$$g = \frac{8\pi^2 N\omega_S}{n^2 c^2 \mu\omega_R \Gamma}\left(\frac{\partial\alpha}{\partial\tilde{Q}}\right)^2 \tag{8}$$

is the steady-state gain coefficient for rotational Raman scattering. The gain coefficient can also be expressed in terms of a spontaneous scattering cross section; however, this gain coefficient can be measured and is known and tabulated for many materials.[7] From Eq. (7), it can be seen that Raman scattering is similar to a pure gain process with an exponential gain coefficient proportional to the pump-laser-intensity-length product. If the pulse width of the pump laser is of the order of the response time of the medium then a steady-state solution is not valid and a transient solution must be used. The above equations can be solved (again assuming a nondepleted pump) to give the transient solution[7]

$$I_S(L,t) = I_S(0,t)\exp\left[2\left(gI_L Lt / \tau_R\right)^{1/2} - t/\tau_R\right] \tag{9}$$

for the intensity of the Stokes field in the medium where $\tau_R = 1/\Gamma$ is the response time for SRRS.

In Eqs. (7) and (9), the most difficult input parameter to model is the noise intensity $I_S(0, t)$ that seeds the interaction at $z = 0$ and grows into the output Stokes signal. This noise intensity is due to spontaneous Raman scattering of pump-laser photons into the Stokes wave. Only those noise photons scattered into a small frequency interval and small solid angle in the forward direction will experience appreciable gain throughout the interaction length. For typical experimental conditions, the pump-laser intensity (I_L^{th}) needed to reach SRRS threshold can be obtained by setting the argument of the exponential in Eq. (9) equal to 30 giving

$$I_L^{th} = \frac{\left(30 + t/\tau_R\right)^2}{4gLt/\tau_R}. \tag{10}$$

This definition of threshold can be interpreted as the pump-laser intensity required for the Stokes intensity to grow to 1% of the pump-laser intensity (i.e., $I_S = 0.01\, I_L{}^{th}$). From this analysis, the noise intensity $I_S(0, t)$ in Eq. (9) that seeds the SRRS process can be approximated as

$$I_S(0,t) = \frac{0.01}{4gLt / \tau_R}\left(30 + t / \tau_R\right)^2 \exp(-30). \tag{11}$$

For short pulses, Eq. (9) with Eq. (11) can be used to approximate the Stokes signal generated by an intense laser beam propagating over a long air path.

The above discussion assumed that the optical fields could be represented as plane waves with slowly varying amplitudes. The analysis should also hold for an input field with a bandwidth $\Delta\,\omega$ due to phase modulation. For the case of a large phase-modulated bandwidth $\Delta\omega >> \tau_R^{-1}$,one should not use $t = \Delta\omega^{-1}$ as the time in the transient gain formula Eq. (9); although the phase of the pump laser is changing with time, the noise field that seeds the Raman process and experiences the highest gain throughout the process will be that which has a phase modulation replicating the phase modulation of the pump laser. Hence, the result is that the threshold for SRRS is independent of bandwidth for a phase-modulated input pump beam.

The above analysis assumed only a single Stokes field was present. In a diatomic gas such as the nitrogen molecules in air, the quantum-selection rules allow the rotational quantum number J to change by 0 and ±2. For $\Delta J = 0$ the gain for SRRS is 0, and for $\Delta J = -2$ the gain is negative. Hence, for positive SRRS gain, only the $\Delta J = +2$ transitions (S transitions) will contribute. The spectrum of SRRS will then consist of discrete lines spaced by

$$\Delta v = 4B\left(J + \frac{3}{2}\right) \tag{12}$$

from the pump laser, where B is the rotational constant equal to 2 cm^{-1} for nitrogen.[1]

Experimental Results

To determine the effects of pure phase-modulated bandwidth on the SRRS process, the gratings in the OMEGA driver line were removed, and the LiNbO$_3$ electro-optic modulator was used to impose a sinusoidal phase modulation with 8.45-GHz modulation frequency onto the beam. This phase-modulated pulse was then amplified by one beamline of the OMEGA laser. The frequency-tripled output from this beamline was down-collimated to a 5-cm beam diameter and propagated over a distance of 35 m in air. At the end of the path the beam was analyzed with a 1-m Spex spectrometer having a 1200-lines/mm grating used in second order. The energy of the beam was varied up to 20 J per pulse and measured with calibrated detectors.

The spectroscopic data was recorded with Kodak Aerographic Duplicating Film 4421 with a peak spectral sensitivity near 350 nm. To calibrate the film, a wedged etalon provided calibrated laser pulses varying in energy. The etalon was coated for 70% reflection on each side, yielding a factor-of-2 change in intensity between successive pulses transmitted through the tilted etalon and sent to the film. The film was then digitized with a microdensitometer and a density-log-intensity (D-log-I) curve was constructed giving a usable peak film density of ~4. This enabled detection of the faint Stokes and anti-Stokes lines while not saturating the fundamental laser line.

A typical Raman spectrum is shown in Fig. 44.8, where the laser line at $\Delta\nu = 0$ was intentionally saturated to better illustrate the SRRS spectrum. In this spectrum, the four strong Raman lines on the Stokes side of the laser can be identified as the S(6), S(8), S(9), and S(10) lines from nitrogen. The corresponding second Stokes and anti-Stokes lines of these transitions can also be seen. In addition to these four lines, several other lines can be identified corresponding to other rotational levels as well as lines due to the scattering off more than one rotational level. Note that odd *J*-value transitions, such as the S(9) and others not previously reported, are clearly seen in the Stokes and anti-Stokes spectra. The overall envelope to this spectrum is due to scattering of the highly saturated laser radiation in the film emulsion. This envelope disappears when the film is not saturated with laser light.

Fig. 44.8
Raman spectrum showing several of the *S* transitions of nitrogen in air. The pump laser saturated the film at $\Delta\nu = 0$.

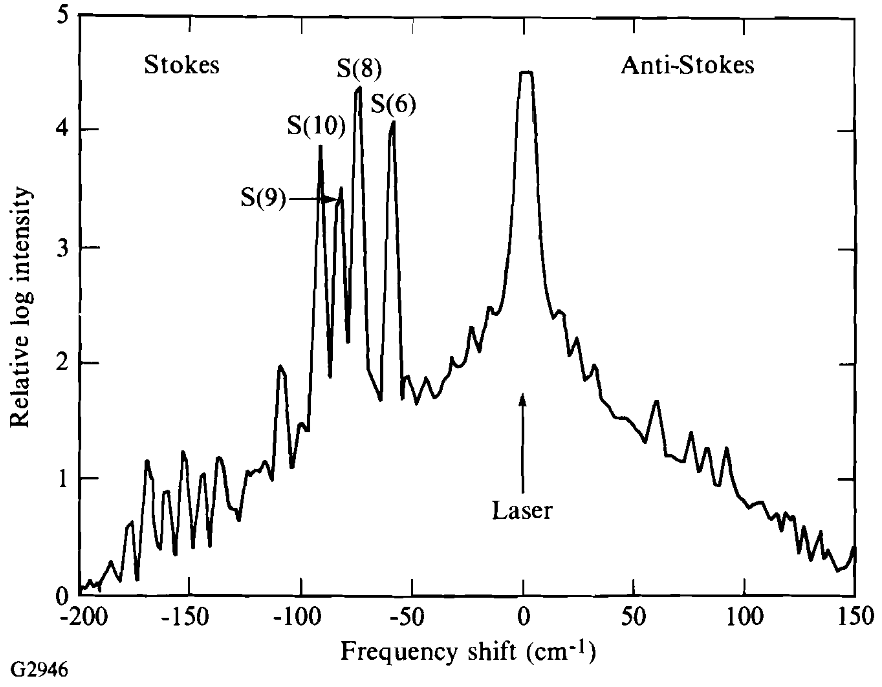

To measure the threshold for SRRS, spectra from several laser pulses were processed to obtain the Raman Stokes energy for each laser pulse. The film was first linearized in intensity using the D-log-I calibration curves described above. The energy on the film was then integrated along the spectrometer exit-slit direction to produce a calibrated intensity profile of the Raman spectra similar to the saturated profile of Fig. 44.8. The area under the laser line on the spectra was then compared to the area under all the Stokes lines giving the ratio of laser energy scattered into all the Stokes lines. The measured laser energy was then used to calculate the energy scattered into all of the Stokes lines.

In Fig. 44.9, the percent of Stokes energy generated is plotted versus the pump-laser-intensity-length product. The near-field intensity profiles of the laser pulses were also recorded on film and indicate that the beam had many intensity "hot spots" within the beam aperture. The laser-intensity-length product plotted in Fig. 44.9 is the laser energy measured with the calibrated detectors, multiplied by the interaction length, divided by the pulse width and beam area, and multiplied by a parameter to account for the intensity hot spots in the beam. In Fig. 44.9, the percent of Raman Stokes energy generated is the ratio of the area under the Stokes lines in the spectra to that of the pump. Figure 44.9 shows the SRRS threshold for three different bandwidths at 351 nm: no phase-modulated bandwidth ($\Delta \lambda = 0\,\mathrm{cm}^{-1}$), 1.37 cm^{-1}, and 4.28 cm^{-1}. The solid curve in Fig. 44.9 is the theoretical calculation of the percent of Stokes energy generated [from Eqs. (9) and (11) assuming the same Stokes pulse width and beam area as the pump laser] plotted versus the pump-laser-intensity-length product.

Fig. 44.9
Threshold for SRRS in air with 0 cm^{-1}, 1.37 cm^{-1}, and 4.28 cm^{-1} of phase-modulated bandwidth.

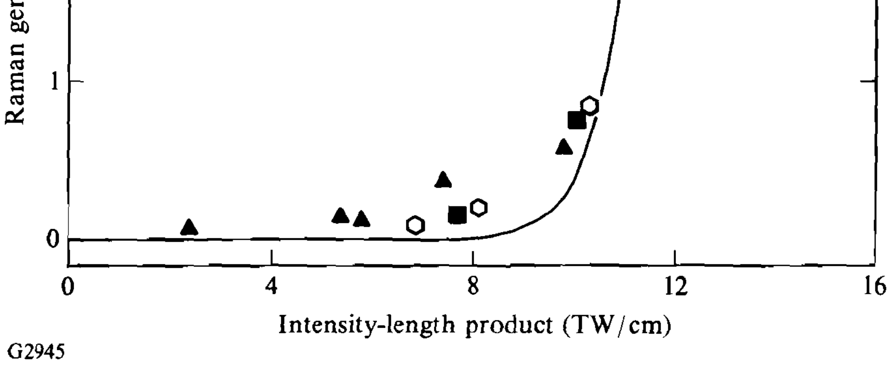

The wavelength dependence of the gain coefficient g has been calculated[3] and for 351 nm in air is ~7.5 cm/TW (see for example, Fig. 2 of Ref. 3). The remaining parameters used in this calculation that give the best fit to the data are $I_S(0, t)$ from Eq. (11), the laser pulse width $t = 500$ ps, the response time for SRRS $\tau_R = 133$ ps,[2,8] and the interaction length $L = 35$ m. A hot-spot parameter of 2 was used for all of the data points. From Fig. 44.9 we note that the threshold for SRRS in air is unaffected by the introduction of up to 4.28 cm^{-1} of phase-modulated bandwidth.

To test the effect of SSD on the SRRS process, SSD was installed on the OMEGA laser and the above experiment was repeated. The angular spectral dispersion of the beam used in the experiment was 74 μrad/cm^{-1} at 351 nm in one dimension at the output of the down collimator. The virtual image of the second grating (after taking into consideration the image relaying throughout the OMEGA beamline and the down collimator) was located at a distance of ~2.5 m before the beginning of the 35-m, down-collimated beam path. For example, with an applied SSD bandwidth of 3.80 cm^{-1} the divergence of the beam is 282 μrad in one direction, due to angular spectral dispersion, and diffraction limited in the orthogonal direction. This bandwidth increases the beam area at the end of the path by ~28% and provides "smoothing" of the beam-intensity profile.[5] All other parameters of the experiment were identical to the pure phase-modulated bandwidth above.

Figure 44.10 shows the threshold for SRRS with and without SSD. In this figure four different bandwidths are shown: no SSD bandwidth ($\Delta\lambda = 0$ cm^{-1}), 1.37 cm^{-1}, 2.18 cm^{-1}, and 3.80 cm^{-1}. To obtain the laser-

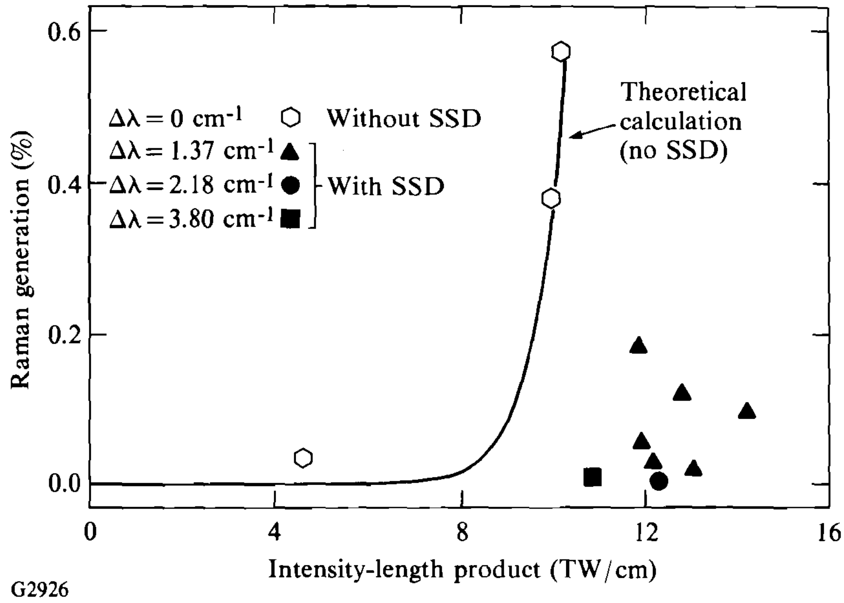

Fig. 44.10
Threshold for SRRS in air with 0 cm^{-1}, 1.37 cm^{-1}, 2.18 cm^{-1}, and 3.80 cm^{-1} of phase-modulated bandwidth with SSD.

intensity-length product for the data in this figure, the laser intensity was integrated over the beam path, i.e.,

$$\int_0^L I_L(z)dz,$$

to account for the applied angular spectral dispersion. For best fit to the data, the same parameters as above were used in the no-bandwidth theoretical calculation (solid curve) and a hot-spot parameter of 3 was used for all of the data points. (Due to the increased divergence of the laser with SSD, larger pinholes were used in the spatial filters resulting in an increase in the intensity modulation of the beam.) It can be seen from Fig. 44.10 that the threshold for SRRS increased for 1.37 cm^{-1} of SSD bandwidth. In addition, for 2.18 cm^{-1} and 3.80 cm^{-1} of SSD bandwidth, no SRRS signal was recorded when the pump laser intensity-length product was above the no-bandwidth threshold for SRRS.

We conclude from the excellent theoretical fit to the data that the simple models for SRRS hold for our experimental conditions. In particular, SRRS generated by the frequency-tripled output from a large Nd:glass laser is seeded by the usual noise mechanisms; a transient solution for laser pulses of 500-ps pulse width is appropriate; and the SRRS gain coefficient is ~7.5 cm/TW at 351 nm. The threshold for SRRS is unaffected by the application of up to 4.28 cm^{-1} of pure phase-modulated bandwidth with 8.45-GHz modulation frequency. The threshold for SRRS, on the other hand, increases with as little as 1.37 cm^{-1} of SSD bandwidth.

ACKNOWLEDGMENT

This work was supported by the U.S. Department of Energy Division of Inertial Fusion under agreement No. DE-FC03-85DP40200 and by the Laser Fusion Feasibility Project at the Laboratory for Laser Energetics, which has the following sponsors: Empire State Electric Energy Research Corporation, New York State Energy Research and Development Authority, Ontario Hydro, and the University of Rochester.

REFERENCES

1. V. S. Averbakh, A. I. Makarov, and V. I. Talanov, *Sov. J. Quantum Electron.* **8**, 472 (1978).
2. M. A. Henesian, C. D. Swift, and J. R. Murray, *Opt. Lett.* **10**, 565 (1985).
3. M. Rokni and A. Flusberg, *IEEE J. Quantum Electron.* **QE-22**, 1102 (1986).
4. A. Ori, B. Nathanson, and M. Rokni, *J. Phys. D: Appl. Phys.* **23**, 142 (1990).
5. S. Skupsky, R. W. Short, T. Kessler, R. S. Craxton, S. Letzring, and J. M. Soures, *J. Appl. Phys.* **66**, 3456 (1989). See also LLE Review **37**, 29 (1988).

6. M. Skeldon and R. Bahr, to be published in *Optics Letters*.
7. W. Kaiser and M. Maier, in *Laser Handbook*, edited by F. T. Arecchi and E. O. Schulz-Dubois (North-Holland Publishing Co., Amsterdam, 1972), Vol. 2, Chap. E2, pp. 1078-1150.
8. K. S. Jammu, G. E. St. John, and H. L. Welsh, *Can. J. Phys.* **44**, 797 (1966).

1.C Energy Transport Measurements in a Multisegmented Amplifier (MSA)

During the last quarter of 1989 final assembly and checkout were performed on the 24-cm-aperture multisegmented amplifier (MSA). The MSA in final assembly is shown in Fig. 44.11. The amplifier consists of two pairs of disk amplifiers, each five disks deep, that share a common central flash-lamp array. The MSA configuration reduces the ratio of reflector material to Nd:glass. Since flash lamps reabsorb and re-emit their own light with less than unity efficiency and reflectors are never perfect, the MSA central array is expected to be more efficient at pumping the disks, thereby raising the amplifier storage efficiency. This is highly desirable for long-pulse laser systems, where system efficiency is of paramount interest and the appropriate figure of merit is dollars-per-focusable joule.

During the course of this work, the importance of power balance on target became known.[1] While the MSA architecture is eminently suitable for a multimegajoule fusion laser facility[2] (such as the NOVA Upgrade) where one MSA amplifies one beam consisting of up to 16 beamlets, in the OMEGA Upgrade one MSA would amplify four independent beams. Because each of these beams requires independent gain adjustability to obtain power balance, which is difficult with the MSA, the decision was made to use single-beam amplifiers in the OMEGA Upgrade. Therefore, the MSA was completed as an important contribution to the NOVA Upgrade and the technology used as a first step in the development of disk amplifiers for the OMEGA Upgrade. Here we report on the energy-transport measurements made on the MSA during the first and second quarters of 1990.

Amplifier Description

The MSA is shown in more detail in Fig. 44.12. The individual 3.3-cm-thick phosphate-glass disks have a 24-cm clear aperture. This is 4 cm larger than necessary for a single beam since the amplifier is designed to be angularly double passed as shown in Fig. 44.13. The angle between the entering and exiting beams is 20 mrad. All testing of the amplifier was performed in this configuration. The disks were elliptically masked presenting a circular aperture to the beams in order to avoid pumping unused glass.

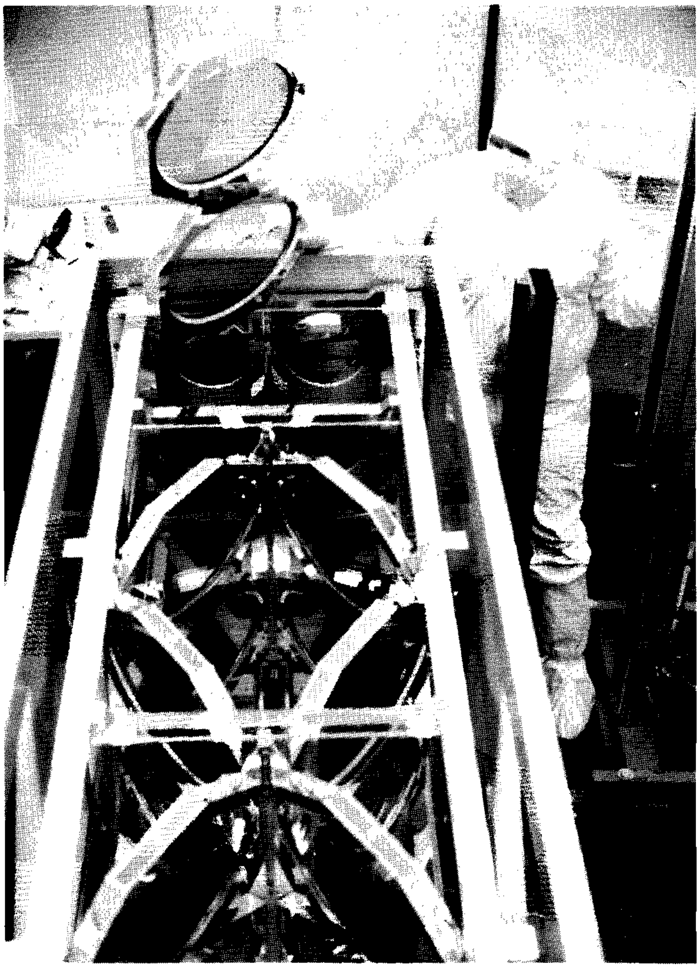

G2878

Fig. 44.11
The MSA amplifier under assembly in a class-100 clean room. A pair of disks in their frame is being lowered into the amplifier. The four apertures are visible at the top of the amplifier frame. Some of the five disks for each beam are visible in the foreground.

The amplifier contains 160 N_2-cooled, 1.9-cm bore Xenon flash lamps with a 58-cm arc length. The lamps are oriented vertically to avoid interference with the disk ends thereby permitting closer packing of the lamps to the disks. There are 80 lamps in the interior array positioned on 1-in. centers and 40 lamps in each of the exterior arrays positioned on 2-in. centers. There are no reflectors between the lamps in the interior array. The lamp-packing fraction is 1.175. Each lamp in the interior array is wrapped with a grounded Nichrome wire to enhance triggering. Blast windows of a water-white float glass 0.25 in. thick are mounted on both sides of the interior arrays and on one side of the exterior arrays. Reflectors are used on only the exterior arrays and are simple searchlight reflectors, the center of each lamp located at one-half of the radius of its individual reflector cusp. The reflectors are dip-coated silver, >95% reflecting over the entire pump spectrum, 400–900 nm.

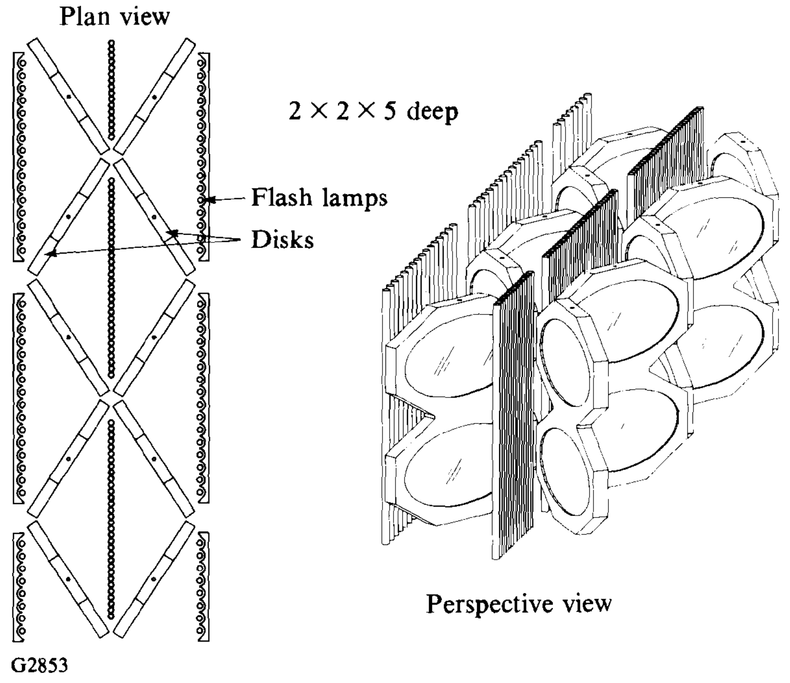

Fig. 44.12
Schematic of the MSA. The top and bottom reflectors and the near-side flash lamps are not shown for clarity. Note that the central flash-lamp array has twice the packing density of the outboard arrays.

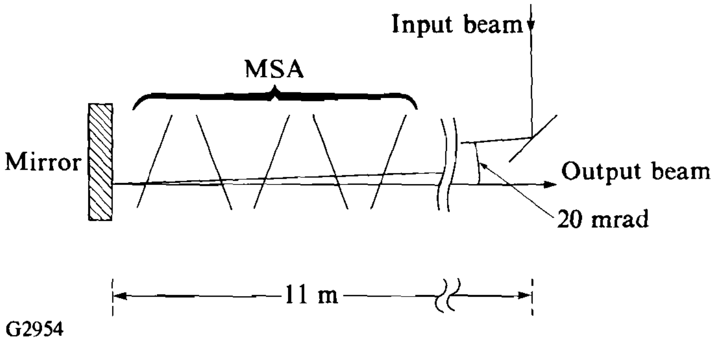

Fig. 44.13
Angular double passing of the MSA. The 11-m propagation distance and the 20-mrad angle between input and output beams allows for a separation of 6.4 cm between beam edges.

Four lamps are connected in series and driven by one pulse forming a network consisting of a 100-μF capacitor and a 278-μH inductor. The lamps are also preionized[3] by a weak discharge initiated 200 μs prior to initiation of the main discharge. The design-charging voltage is 21.5 kV for a total nominal capacitor-bank energy of 924 kJ. This bank energy will be referred to as "100% nominal bank energy" throughout the remainder of this article.

Experimental

Two sets of energy-transport measurements were made: small- and large-signal gain. These can be self-consistency checked with a Frantz-Nodvik[4] model of the amplifier, coupled with a knowledge of the losses in the amplifier. These measurements were done as a function of percent bank energy. This yielded valuable information on the dynamics of the pumping process.

The small-signal gain was measured with the apparatus shown in Fig. 44.14. This apparatus measures the small-signal gain at three locations in one of the clear apertures. In all of the measurements reported here the small-signal gain was measured in the plane of incidence of the disks (horizontal). The locations were the center of the clear aperture and 1.0 cm from the edge of the clear aperture. A polarized cw Nd:YLF oscillator operating on the 1.054-μm transition is split three ways. Each of the three beams then double passes the amplifier. The return beam is first dispersed with a grating to reduce the spectrally near fluorescence. The beam is then reflected from a 1-μm mirror to limit the amount of flash-lamp light seen by the detector. Each beam is spatially filtered with a 1-mrad cutoff full angle before detection to further limit both fluorescent light and lamp light. Large-area photodiodes with a measured $1/e$ response time of 2 μs detected the signals. A fourth identical photodiode monitored the Nd:YLF laser output as a reference.

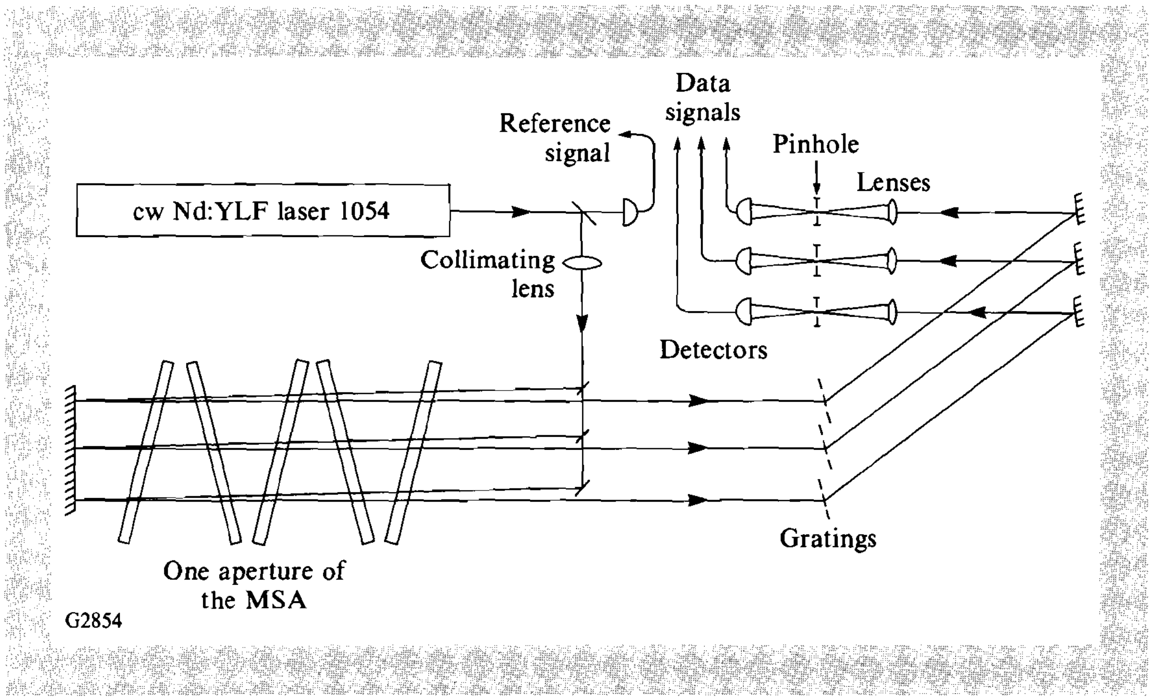

Fig. 44.14
Schematic of the small-signal-gain measurement apparatus. The cw Nd:YLF laser is split into three beams that probe different locations within the *same* aperture. The return signals are filtered spectrally with gratings and spatially filtered before detection.

Signals from the large-area photodiodes were digitized by Tektronix[5] 2440 oscilloscopes with 500 megasample-per-second maximum-digitizing rate. Signals were digitized into 2-ms, 1024 sample-record lengths with 8-bit amplitude resolution. The 2.0-ms record length ensured that the entire temporal history of the gain and a portion of all signals prior to the initiation of the flash-lamp discharge were recorded. The signals were then Fourier transformed, filtered with a Blackman[6] filter whose cutoff frequency was 100 kHz. A background "shot" was taken for each gain measurement. For the background shot, the cavity of the Nd:YLF was blocked and all of the above signals were recorded. This background included fluorescence from the amplifier and any non-cancelling noise. The background for each channel was subtracted from the data for that channel. The temporal variations of the Nd:YLF were removed by dividing each of the three signal channels by the reference channel. A 200-μs sample of each of the three channels prior to initiation of discharge was averaged and set equal to unity. The remainder of the data in that channel was multiplied by the so-determined constant to convert the data to small-signal gain. The estimated precision attained as a result of this procedure is ±1%. The gain of a reference 90-mm-rod amplifier could be routinely remeasured with this precision.

For the large-signal-gain measurements the amplifier was deployed on the OMEGA laser system as shown in Fig. 44.15. The output of the OMEGA 90-mm-diam rods, after expansion to 160 mm by the output spatial filter, was turned 90° and further expanded to 180 mm by a Galilean expander. The 180-mm beam was turned 90° and double passed the amplifier. The output of the amplifier was spatially filtered in an *f*/14 spatial filter with a 475-μrad full-angle cutoff. The input and output energies were measured calorimetrically.[7] The input energy was taken from an uncoated pickoff prior to the Galilean upcollimator. The output energy was taken from a similar uncoated pickoff after the *f*/14 output spatial filter.

Results

The measured small-signal gain at three positions within one aperture of the MSA as a function of percent of nominal bank energy is shown in Fig.

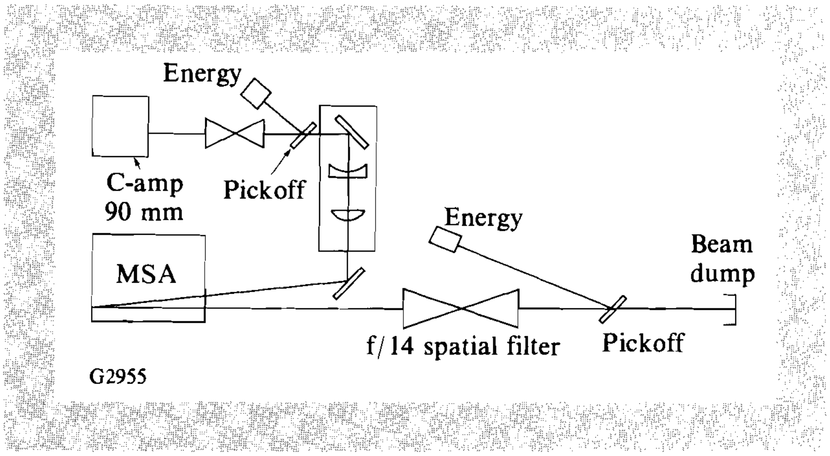

Fig. 44.15
Schematic of the large-signal-gain experiment. The 90-mm output of beamline 6-2 of the OMEGA laser system was magnified by 2, turned, further magnified by 1.10, and turned into the amplifier. The output of the amplifier was spatially filtered by an *f*/14 filter with a 475-μrad full-angle cutoff.

44.16. The small-signal design goal of 11.8 in double-pass was achieved at ~65% of the nominal bank energy. The center of the aperture consistently displayed the highest gain. The edge of the aperture closest to the interior array was slightly higher in gain than the outboard array, lending support to reports[8] that the interior arrays are more efficient in pumping Nd^{+3}. At high percentages of nominal bank energy, the main discharge often initiated before completion of the preionization. This reduced the maximum achieved gain and is in part responsible for the deviation from linearity in Fig. 44.16.

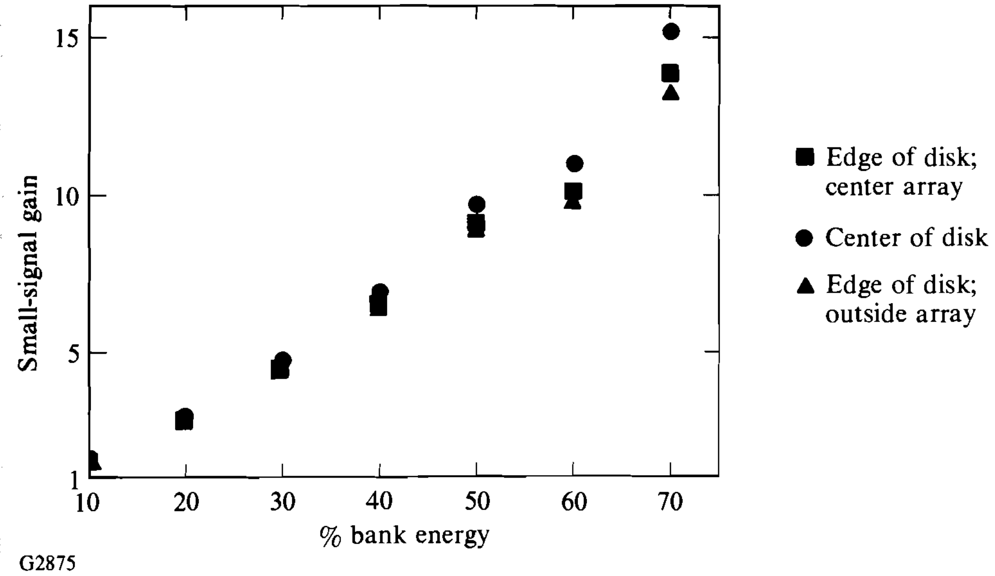

Fig. 44.16
The small-signal gain of the three locations plotted versus percent nominal bank energy. The small-signal design goal of 11.8 was achieved at 65% of the design-bank energy.

The overall storage efficiency, defined as stored energy in the glass divided by the stored energy on the capacitor bank, is shown in Fig. 44.17 plotted versus the stored fluence per disk. The stored fluence per disk is the stored energy-per-unit-beam-area per disk. Also shown on this same plot is the performance of several other disk amplifiers, both standard box design and MSA. All of these plots are based on an assumed stimulated-emission cross section of 3.5×10^{-20} cm^2. The plot displays the characteristic high-cavity efficiency at lower lamp loadings due to reduced cavity opacity and declining efficiency as the gain increases, the cavity opacity increases, and amplified spontaneous emission (ASE) begins to become significant. The high cavity-transfer efficiency near the design goal of 2.06 J/cm^2 (0.34 J/cm^3) is particularly surprising since this MSA used a

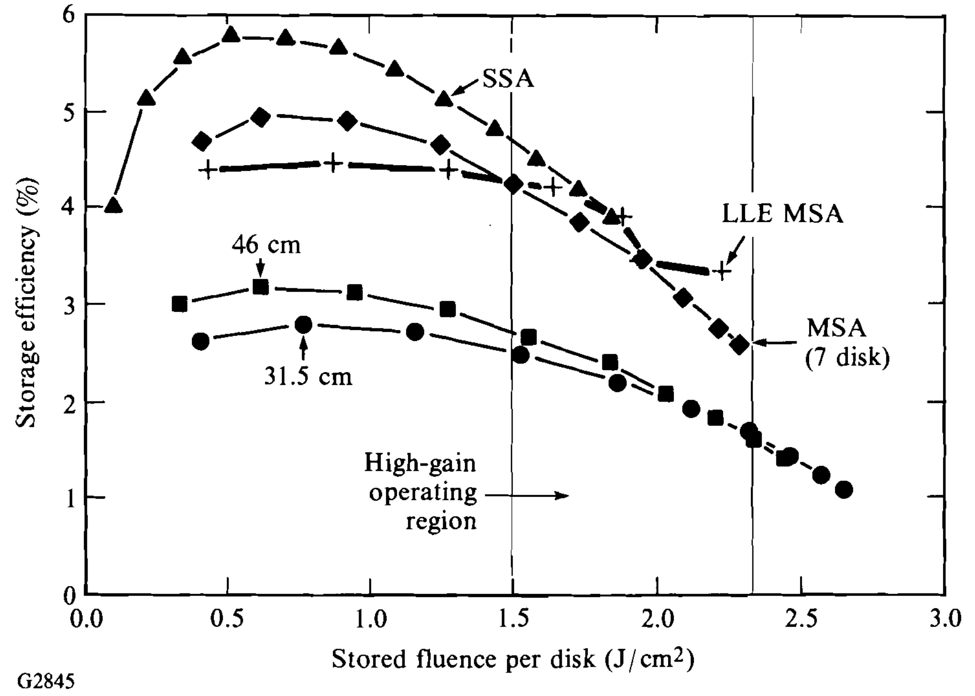

Fig. 44.17
Disk-amplifier storage efficiencies plotted versus the stored fluence per disk. The stored fluence per disk is the stored energy-per-unit-beam-area per disk. The MSA architecture is very efficient relative to other disk amplifiers in the region of interest around 2.0 J/cm^2.

circular clear aperture instead of a square clear aperture. It is evident that the improved packing and reduced losses of the MSA architecture can result in improved amplifier efficiency.

The large-signal gain of the MSA plotted versus percent nominal bank energy is shown in Fig. 44.18. The drive into the amplifier from the OMEGA laser system was held constant at 130±6 J for this series. An output of 950 J was achieved at 70% of nominal bank energy. This actually outperformed the design goal of 1000-J output with 185-J drive at 100% of nominal bank energy.

One additional observation not widely reported previously was that for a period of 1 to 2 s following a high bank-energy shot, the amplifier cavity was observed to glow with a bluish color. The glow decayed slowly enough to permit photographing the amplifier using no other light source. It is presently hypothesized that the glow is due to the auroral bands of N_2.

Conclusion

The MSA has been demonstrated at full scale as a particularly efficient amplifier. Storage efficiencies in excess of 4% have been achieved with good gain uniformity. These measurements support the choice of the MSA architecture for an LMF-scale facility.

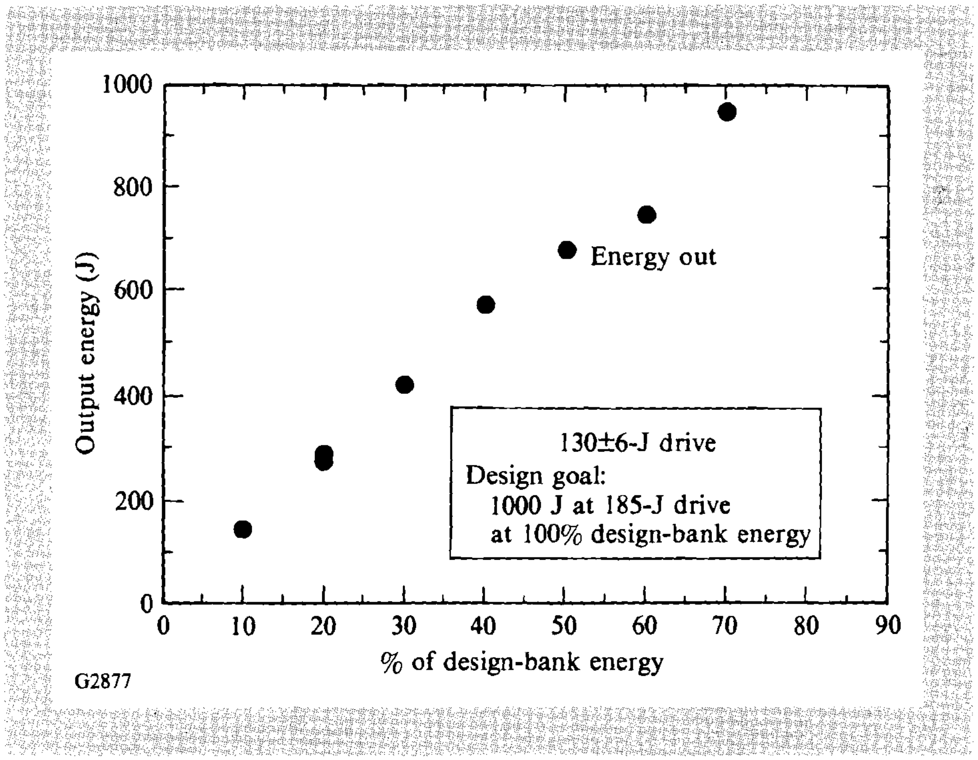

Fig. 44.18
MSA energy output plotted versus percent of the design-bank energy. The MSA achieved 950-J output with 130-J drive at only 70% of the design-bank energy. The design goal was 1000-J output with 185-J drive at 100% of design-bank energy.

ACKNOWLEDGMENT

This work was supported by the U.S. Department of Energy Division of Inertial Fusion under agreement No. DE-FC03-85DP40200.

REFERENCES

1. LLE Review **41**, 4 (1989).
2. Lawrence Livermore National Laboratory, Laboratory Inertial Confinement Fusion Program, Precision NOVA and NOVA Upgrade Laser, NOVA Upgrade Campaign, Book 2 (1990).
3. Laser Program Annual Report 1985, Lawrence Livermore National Laboratory, UCRL 50021-85 (1986), pp. 7-18–7-24.
4. L. M. Frantz and J. S. Nodvik, *J. Appl. Phys.* **34**, 2346 (1963).
5. Tektronix Inc., Beaverton, Oregon, USA.
6. R. B. Blackman and J. W. Tukey, *The Measurement of Power Spectra* (Dover Publishing, New York, 1958).
7. OMEGA Upgrade Preliminary Design Document, DOE/DP40200-101, p. 9.17 (1989).
8. A. C. Erlandson, H. T. Powell, and R. W. McCracken, Lawrence Livermore National Laboratory, UCRL-ID-104157 (1990).

1.D Disk Amplifier Design for the OMEGA Upgrade

The OMEGA Upgrade will use as its final amplifier a disk amplifier with a single 20-cm clear aperture as shown in Fig. 44.19. A single-, rather than a multiple-aperture amplifier such as the multisegmented amplifier (MSA), is chosen in order to permit adjustment of individual amplifier gains for power balance[1] on target. This final amplifier is designed with several unique goals in mind. First, in keeping with LLE's direct-drive mission, it must have superior wave-front and polarization characteristics. Second, because of the anticipated pulse widths in the OMEGA Upgrade, it must be a short-pulse amplifier; that is, it must emphasize gain over efficiency. Third, it must be designed for minimum maintenance over a lifetime in excess of 20,000 shots. A prototype amplifier has been designed that incorporates the best aspects of existing designs[2,3] and, in addition, makes some significant improvements. This article describes that amplifier and its projected performance.

Requirements

The 20-cm amplifier is driven by a 15-cm, four-disk amplifier. In this configuration it is required to produce 855 J in an 800-ps main pulse and, simultaneously, 200 J in a 5-ns foot pulse by use of co-propagation.[4] It must do this with 370-J drive for the main pulse and 85-J drive for the foot pulse. The first photon gain of the amplifier is required to be 3.0. These requirements are calculated by using a simple Frantz-Nodvik[5] model of a saturating amplifier with a saturation fluence of 3.75 J/cm^2. Storage efficiency, while not as important a consideration as gain-per-unit path in glass, should not be less than 1% for cost considerations. Passive losses are specified to give the amplifier a 96% transmission.

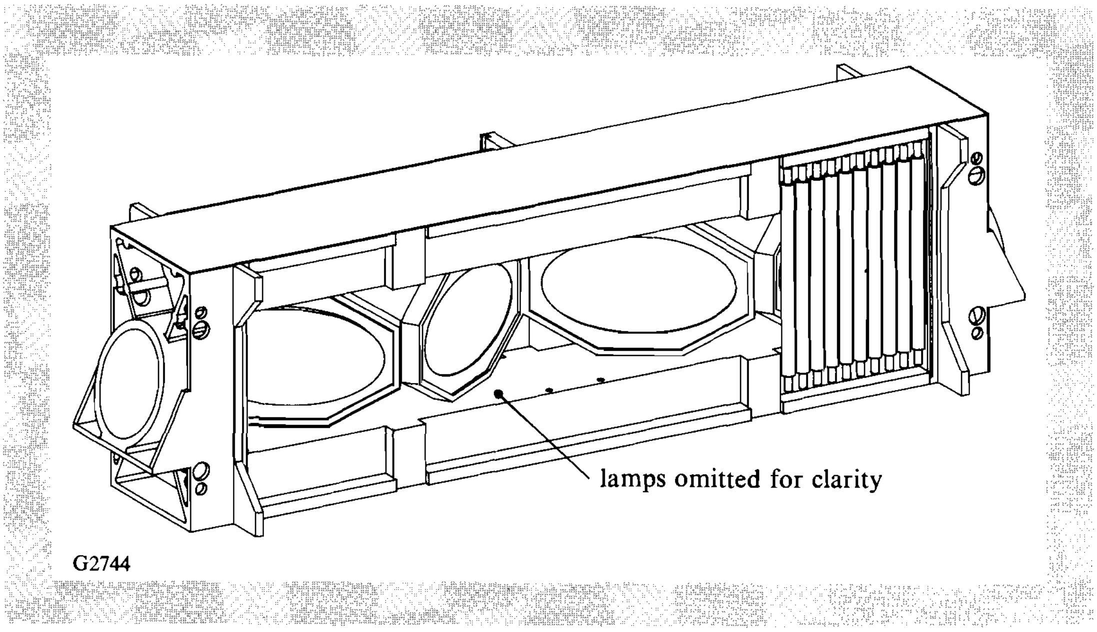

Fig. 44.19
The 20-cm, four-disk amplifier. Note that the transverse flash lamps have been removed for clarity.

The amplifier wave front is expected to be no worse than 0.35 λ rms at 1 μm. In addition to the amplifier wave front at the gain peak (prompt wave front), longer-term (~1-h or steady-state) variations due to post-shot radiative exchange and cumulative shot effects must be minimized in order to meet a one-shot-per-hour repetition rate. Current OMEGA operations are in excess of this rate and the upgrade is planned to be comparable to present OMEGA operations.

Birefringence in the amplifier manifests itself as a spatial beam-intensity modulation and a passive loss both in the amplifier and at the frequency-conversion crystals. The specification of 3.0 nm/cm is driven by the stringent requirement for 3×10^{-4} fractional depolarization at the frequency-conversion crystals. The specification of 3.0 nm/cm is an optimum chosen between what is available at reasonable cost from vendors and the contrast and additional cost of a large-aperture polarizer at the frequency convertors. Birefringence, especially cumulative, also affects the repetition rate.

Finally, although it is difficult to quantify, longevity is a major goal. This, understandably, has its origins in the requirement for high laser availability with low operating costs. There are a number of aspects to amplifier longevity. They include cleanliness, ease of routine service, and solarization resistance. Furthermore, adequate diagnostic capability must be built into the system in order to accurately identify problems should they arise.

Amplifier Description

The amplifier consists of four disks of 3 wt% Nd:phosphate glass, 3.0 cm thick. An even number of disks was chosen in order to obtain adequate gain at the 3.0-cm thickness. The 3.0-cm thickness, 3.0-wt% doping, and 550-μs pump pulse width are optimized for high-gain-per-unit path in glass in order to minimize B-integral. A diagram of a disk is shown in Fig. 44.20. The disk is octagonal with 30° and 60° corners. The disk is clad with 1-μm-absorbing, Cu-doped phosphate glass using a polymer-bonding technique.[6] The thickness of the cladding glass has been increased to 0.8 cm for an absorption-thickness product of 2.8 (3.5-cm^{-1} absorption). Distributing the amplified spontaneous emission (ASE) energy over a greater thickness reduces the peak cladding temperature rise during a shot, thereby reducing the stress on the bond to the laser glass and the deformation induced in the laser glass by the expanding cladding.[7] Superimposed on the disk in Fig. 44.20 is the elliptical projection of the clear aperture. In the LLE design, additional laser glass (2.5 cm) has been left between the top and bottom edge of the clear aperture and the cladding in order to remove the area of greatest beam steering from the clear aperture.

The laser disk is held in a disk frame (Fig. 44.21) that is an octagonal ring of 6061-T6 aluminum, the same depth as the minimum disk thickness. The disk rests directly on the bottom inside of the ring. One side of the ring has a lip that forms the disk mask on one side of the disk. A disk mask is attached

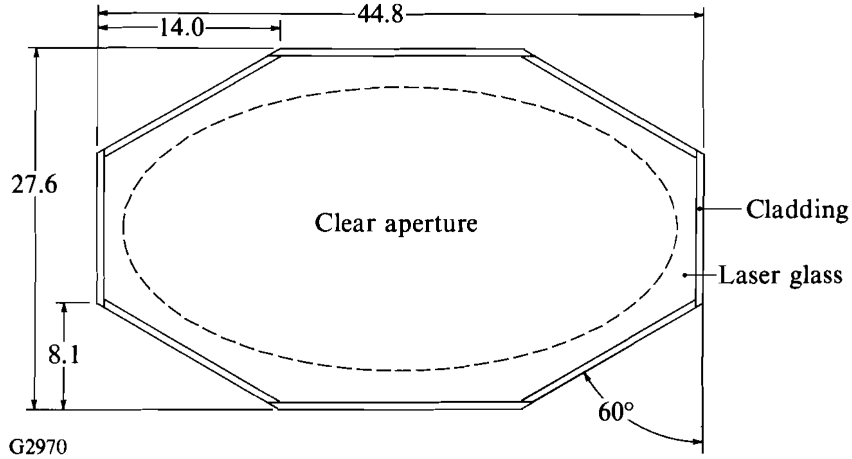

Fig. 44.20
The clad 20-cm laser disk. The location of the clear aperture is marked by the ellipse on the disk face.

Fig. 44.21
The disk frame. The disk frame supports the disk and shields the cladding and extra laser glass from flash-lamp light.

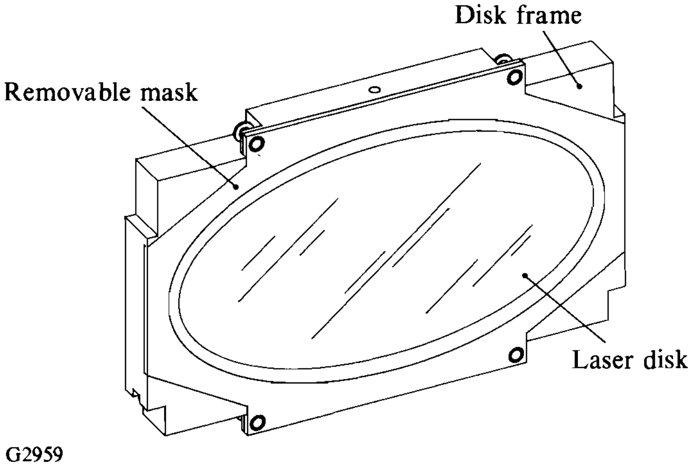

to the opposite side of the ring with four clevis-pin-held springs.[8] The force exerted by the removable mask just equals the weight of the disk. Side-to-side motion of the disk is prevented by marcel springs. The complete spring loading of the disk insulates it from any mounting-induced deformations; in essence, the disk defines its own plane. To further alleviate any potential mounting deformations, the disk frame is mounted into the amplifier frame using a three-point kinematic mount.

The amplifier frame is a four-part casting consisting of top, bottom, and end plates. End plates are pinned and bolted to the top and bottom plates.

The material is aluminum for lightness and ease of manufacturing. Stiffening ribs have been strategically located to reduce part bending and frame "torquing." Vertical members connect the top and bottom plates at locations along the side of the amplifier where disk frame edges meet. V-groove blocks that support the disk frames bolt to the verticals. By separating the frame into four pieces acceptable rigidity is obtained with greatly improved ease of cleaning, assembly, and manufacturing. Disk frame assemblies containing the glass disks are easily loaded into the amplifier frame from the sides. The top and bottom frame members are covered by curved sheet-metal reflectors that are convex into the amplifier volume. Purge gas (clean N_2 or clean air) is introduced into the amplifier cavity behind the upper reflector. Protective blast windows mount to the sides of the amplifier frame. These windows reflect the acoustic wave generated by firing the flash-lamp arrays and isolate the clean interior of the amplifier.

Pump modules (Fig. 44.22) containing the flash lamps and their reflectors attach to the sides of the amplifier over the blast windows. Pump modules are either short or long types depending on whether a module pumps one or two disks. The modules are designed to unlatch and tilt away from the amplifier for *in-situ* replacement of failed flash lamps. (The amplifier stays in place while a lamp module is replaced.) A long module

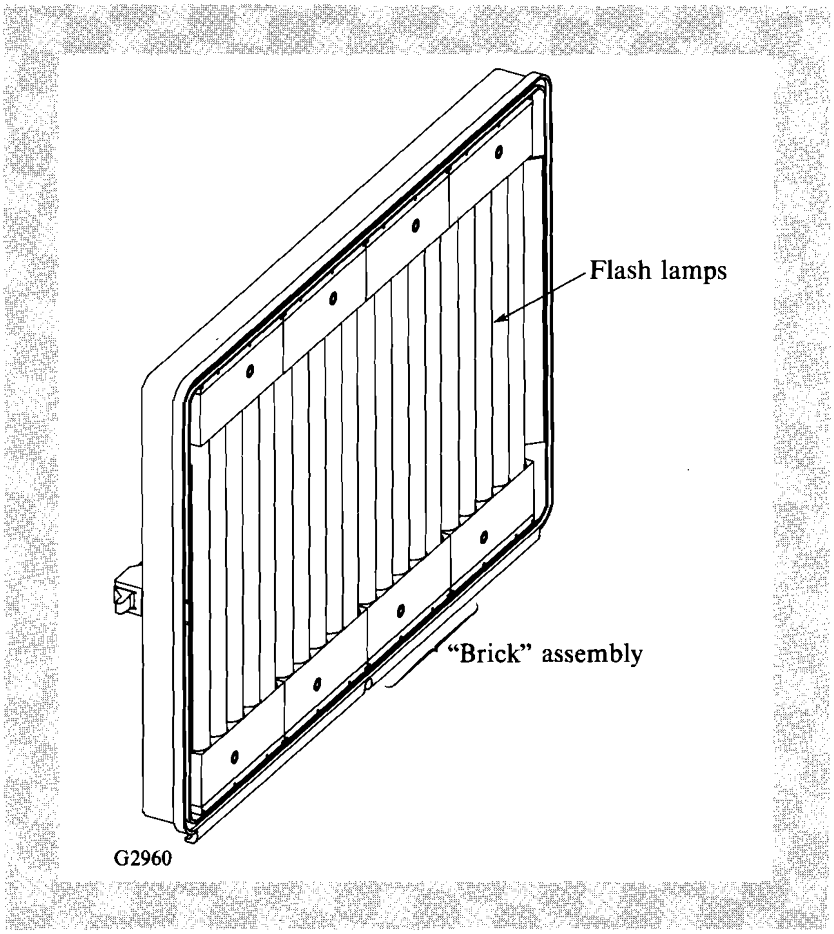

Fig. 44.22
The long-pump module. The long-pump module contains four brick assemblies of five flash lamps each. A simple flat reflector is behind the bricks. The pump module is purged with N_2. The short-pump module is similar but contains only 10 lamps.

contains 20 lamps and a short module contains 10, for a total of 80 transverse-mounted lamps in the amplifier. The lamps are mounted on 1.341-in. centers. Five lamps are connected in series to make a brick. One pulse-forming network (PFN) drives one brick. The individual lamps are 1.9-cm bore with a 10-in. arc length. The lamps are water cooled and cooling is series connected within a brick. A brick is the smallest serviceable component on the in-system amplifier. New brick assemblies are built up off-line in a clean room and are readily installed into amplifiers that may be as high as 3.5 m above the laser bay floor. Simple flat reflectors are used in the pump module because of the close spacing of the water-jacketed lamps.

Water cooling of flash lamps has been retrofitted into existing disk amplifiers at other laboratories.[9] Water cooling has been specified in this amplifier for a number of reasons. First, it virtually eliminates catastrophic lamp failures without having to test every lamp for infant mortality. Second, it allows the use of much-lower-cost lamp-seal technologies such as solder-seal or hard-seal lamps instead of reentrant- or reverse-reentrant-seal lamps. Third, it eliminates the post-shot thermal-soak problem where heat from the lamp walls is radiatively transported to the laser disks causing additional disk deformation. Fourth, in high-voltage systems, deionized water is an excellent insulator, eliminating corona and flashover problems.[10] Deionized water has also been successfully used on the rod-geometry amplifiers in the current OMEGA laser system.

Transverse mounting permits locating the lamps much closer to the disks than is possible with longitudinal lamps. This is especially true since the disks have extra glass and concomitant larger holders in order to keep cladding-induced disk deformations out of the clear aperture. Ray-tracing calculations indicate that the improvement in a new (i.e., untarnished reflectors) amplifier is ~4% in stored energy density for transverse versus longitudinal lamps. The difference between transverse and longitudinal efficiencies can be expected to increase with amplifier age. The transverse mounting with its compact 8 × 21 × 2-in. flash-lamp brick is also vastly more serviceable than the 1 × 65-in. glass and quartz assemblies that would be required for the longitudinal case. Furthermore, the vertical mounting of the lamps avoids the horizontal, longitudinal case tendency of the water jacket to sink and the flash lamp to float.

Each flash-lamp brick is driven by a single-mesh L-C circuit of 210 μF and 160 μH. Nominal charging voltage is 14.1 kV. The same pulse-forming networks will be used for the 15-cm disk amplifier. The lamps will be triggered by "ringing up" the lamp-cable capacitance. The PFN's are individually equipped with current monitors so that misfiring bricks may be readily identified. In addition to the main discharge, all lamps will be preionized[11] 100–200 μs prior to the initiation of the main discharge in order to increase Nd^{+3}-pumping efficiency, reduce hard-UV emission, and reduce lamp-wall stresses.

Calculated Amplifier Performance

Calculations made to estimate amplifier performance have concentrated on beam-quality issues associated with the amplifier: gain uniformity, beam steering, focusing, etc. Gain uniformity and disk deformation require a knowledge of the spatial distribution of either heat or inversion throughout the amplifier. Monte-Carlo pump-light ray tracing[12,13] has provided a useful tool to determine the spatial distribution of inversion. Using the proportionality constant χ,[14] the deposited heat may also be estimated.

Symmetry in the amplifier can be used to reduce the ray-tracing problem to only one quadrant of the amplifier. Two million rays at 200 wavelengths are traced in a typical single-quadrant calculation. *S* and *P* average polarization properties are used. Arbitrary reflection/refraction properties may be assigned to surfaces. Similarly, arbitrary absorption/emission characteristics may be assigned to any volume. The capability to model spectral shifts is important in estimating aging effects where materials solarize, reflectors tarnish, etc.

The ray-tracing results show that the two interior disks are much more uniformly pumped than the two end disks. This is shown in Figs. 44.23(a) and 44.23(b). The plot is of average relative stored-energy density for each cm of the 3-cm disk thickness. The large variation across the disk thickness is of little importance because the beam propagates across this gradient. The variation along the disk major axis is, however, critical. This determines the gain uniformity across the clear aperture of the amplifier and the disk bending. The two innermost (interior) disks are uniformly pumped across the major axis to within the error bars of the code ±8%. The majority of the gain variation and disk bending comes from the two end (exterior) disks, which exhibit a 40% variation across their exterior sides. The thickness-averaged stored-energy density is more uniform resulting in less aperture variation.

The normalized, calculated, small-signal gain profile for the amplifier is shown in Fig. 44.24. The 15% variation from side to side in the horizontal direction is typical of disk amplifiers with an even number of disks.[15] The gain variation in the vertical direction is typically at least a factor of 3 smaller. The horizontal gain variation can be significantly flattened by orienting the 15-cm-driver disk amplifier to have its "hot" side in series with the 20-cm cold side. The resultant stage small-signal gain profile is shown in Fig. 44.25.

Since the deposited heat is, to first order, proportional to the stored-energy density, the calculated stored-energy profile may be used as input to a model of the disk surface displacement. A two-dimensional model of the disk cross section on the major axis was constructed. The deposited heat was assumed to be identically zero outside of the disk clear aperture. This model used the plane-strain approximation wherein the disk is assumed to be infinite in the vertical direction. Spring-support boundary conditions were used on the disk edges in simulation to model the actual disk mounting as accurately as possible. The biharmonic equation[16] was then solved for the Airy stress potential[17] via a finite-element method. Linear elastic-constitutive relations of the glass are used to obtain the displacement field. The solution was checked to ensure that the boundary conditions were satisfied.

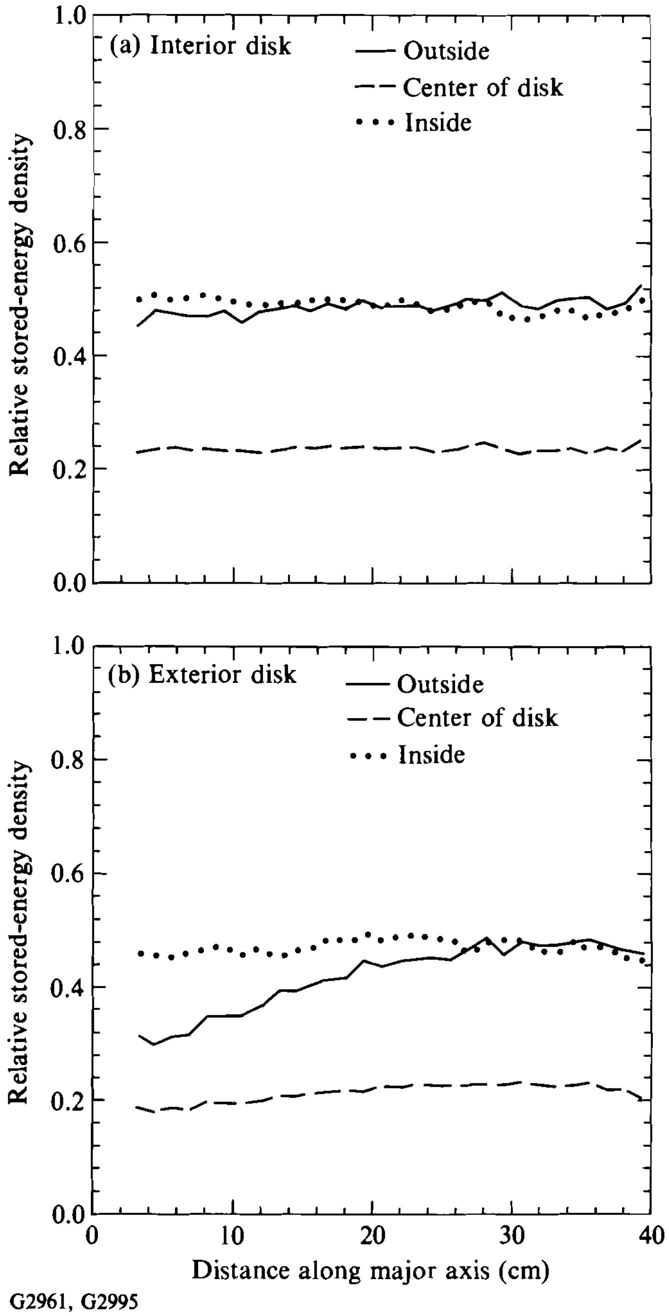

Fig. 44.23
Calculated relative stored-energy density along the major axis of the interior (a) and exterior (b) disks. Variation along the major axis affects disk bending and gain uniformity. The large variation across the disk thickness is unimportant. The interior disk is uniform to within ±8% along the major axis. The change along the major axis of the exterior disk will account for nearly all of the amplifier's gain asymmetry and wave front.

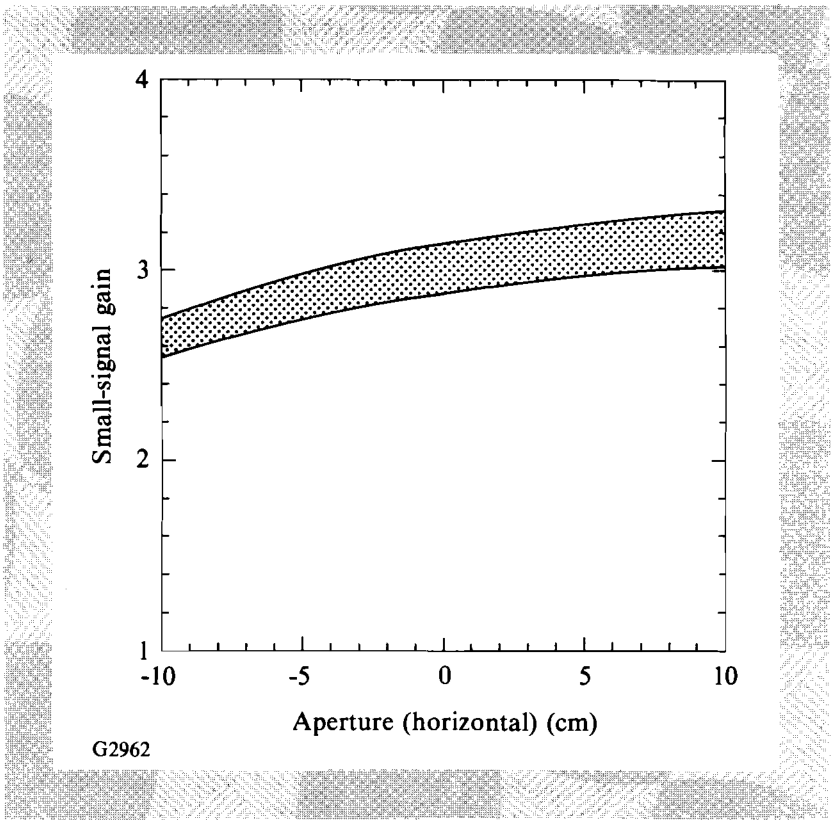

Fig. 44.24
Calculated small-signal gain of the 20-cm amplifier versus aperture.

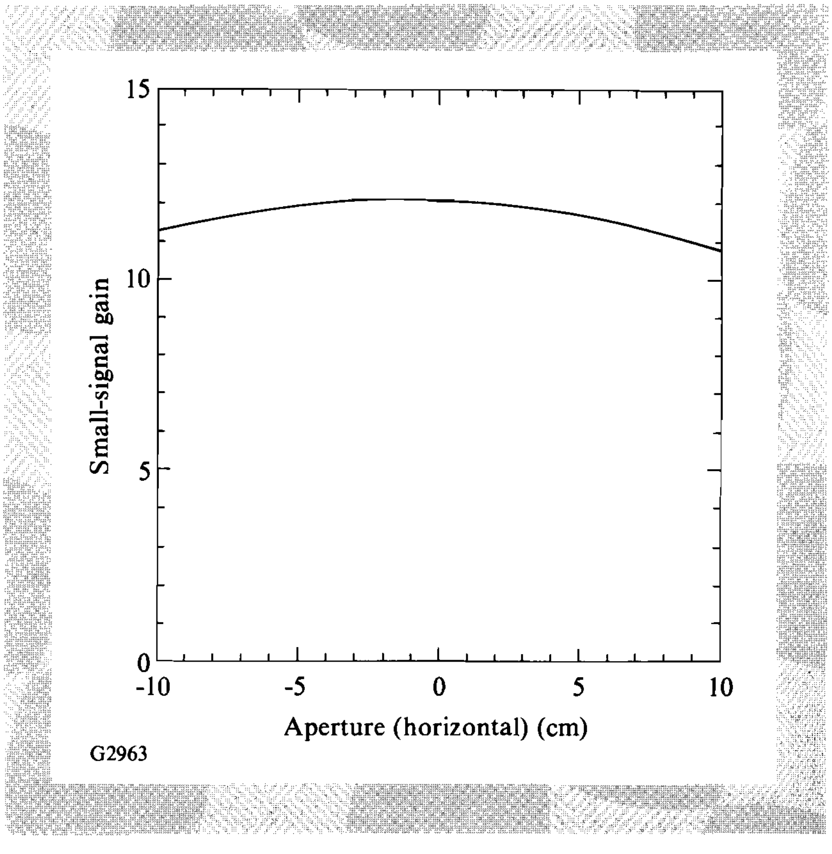

Fig. 44.25
Calculated combined small-signal gain of the 15- and 20-cm amplifiers. The resultant gain is uniform to within ±7%.

If the displacements of the two surfaces are nearly parallel the effect is a bending of the disk (excepting the trivial case of a uniform expansion of the disk). The sensitivity to bending is greatly increased because the disk is at Brewster's angle (see Fig. 44.26). A bending of the disk in the plane of incidence to a constant radius of curvature causes a whole-beam steering. Any variations in the radius of curvature cause higher-order aberrations. These conclusions assume that the coefficient of optical path for the glass is small ($<1.0 \times 10^{-6}$ °C) and that stress-optic effects are negligible. The beam steering δ is given by[18]

$$\delta = \frac{n^2 - 1}{n} \frac{t}{R},$$

where n is the refractive index, t is the disk thickness, and R is the radius of curvature of the bent disk.

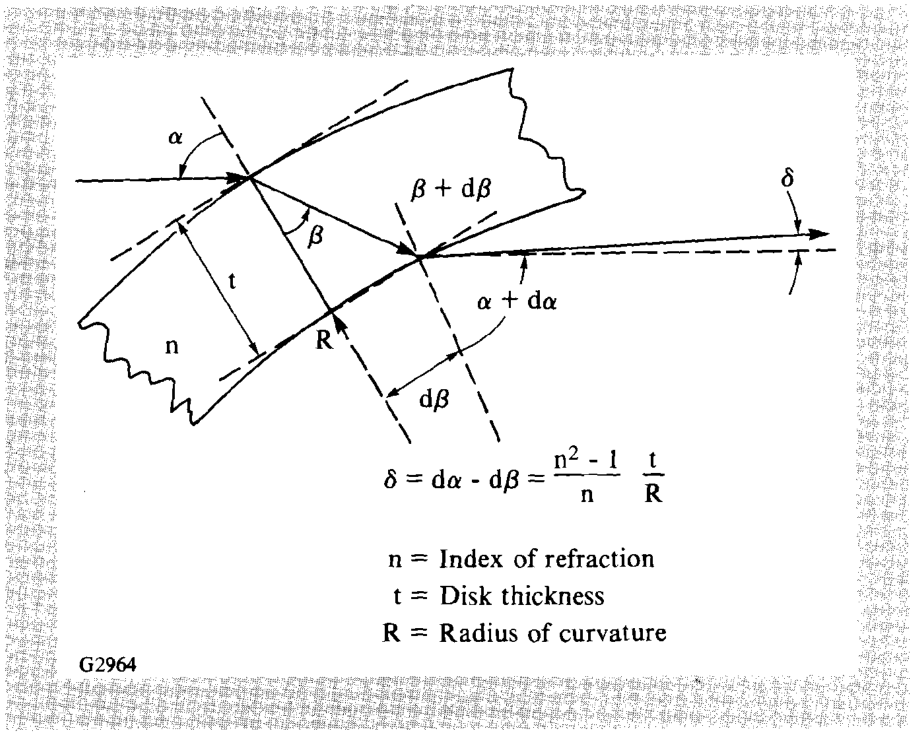

Fig. 44.26
Beam steering due to disk bending.

A plot of surface displacements for the end disks is shown in Fig. 44.27. For this set of conditions the disk displacements are small (~1 μm) and the disk bends with the concave surface out (toward the end of the amplifier). The associated wave front for the amplifier is shown in Fig. 44.28 and is seen to consist of primarily a beam steering in the horizontal plane (~2.5 μrad) and a very weak astigmatism. Note that these results were obtained with a two-dimensional model. Work is continuing on a three-dimensional model to determine the surface displacements along the vertical direction.

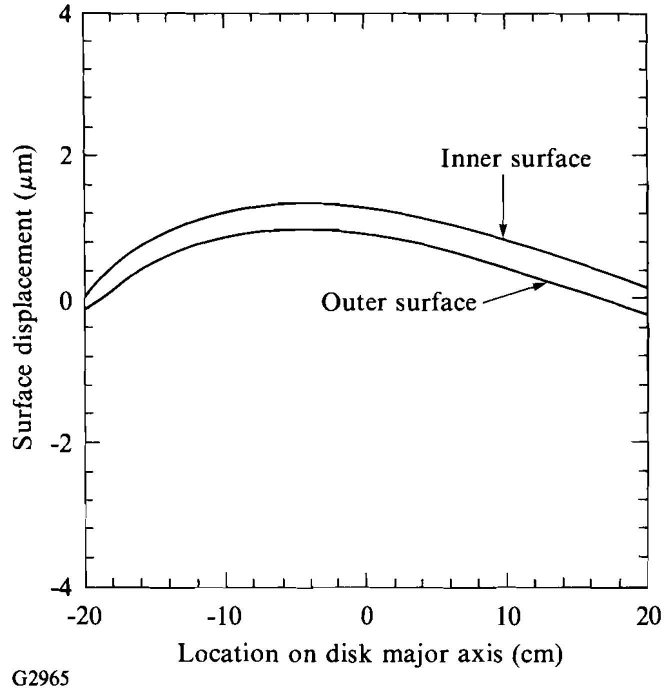

Fig. 44.27
Surface displacement in microns versus aperture in the horizontal direction. The outside of the amplifier is down in this diagram.

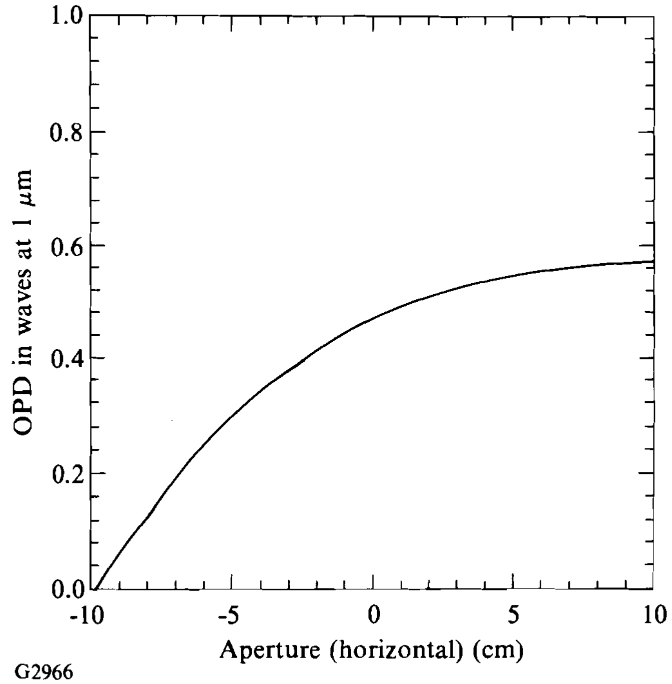

Fig. 44.28
The calculated wave front in the horizontal direction due to prompt disk bending. The beam propagates up in this diagram. The wave front consists primarily of a pointing change and an astigmatic component.

Beam steering due to ASE heating of the cladding glass is not anticipated to be a problem during a shot. The results of a calculation of the surface displacement induced by the cladding expansion is shown in Fig. 44.29. The previously described extra 2.5 cm of laser glass removes the distorted region from the clear aperture. Further calculations are underway to assess the heat removal from the cladding region through the disk masks.

The prompt thermally induced bending of the disks is not the only contributor to the wave-front error of the amplifier. Disk-finishing errors, acoustic effects, etc., also occur. One realization of the passive wave front of the amplifier due to finishing errors is shown in Fig. 44.30 where the interferometrically measured[19] passive wave fronts of four of the MSA disks were added to estimate the passive wave front of the single-segmented amplifier (SSA). The MSA disks are slightly thicker (3.3 cm versus 3.0 cm) and slightly larger (24-cm versus 20-cm clear aperture). Therefore, the resultant summation will be a slightly conservative estimate of the passive wave front. The wave-front rolloff near the edge in the horizontal direction is characteristic of polishing finite plates. The peak-to-valley wave front is ~0.25 λ at 1 μm, substantially below the specification for total wave front (both active and passive).

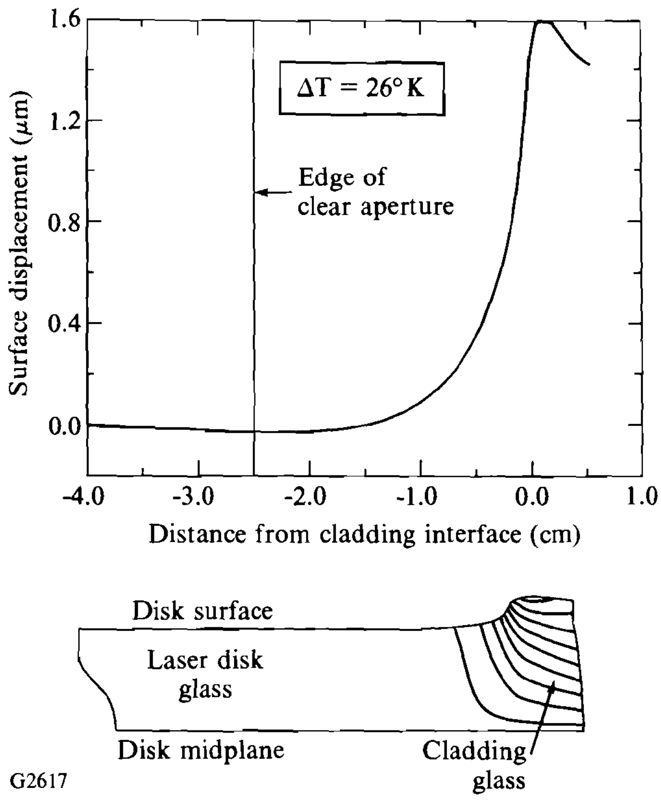

Fig. 44.29
The calculated surface displacement due to heated cladding. The edge of the clear aperture, indicated in the diagram, is well removed from the region of greatest steering.

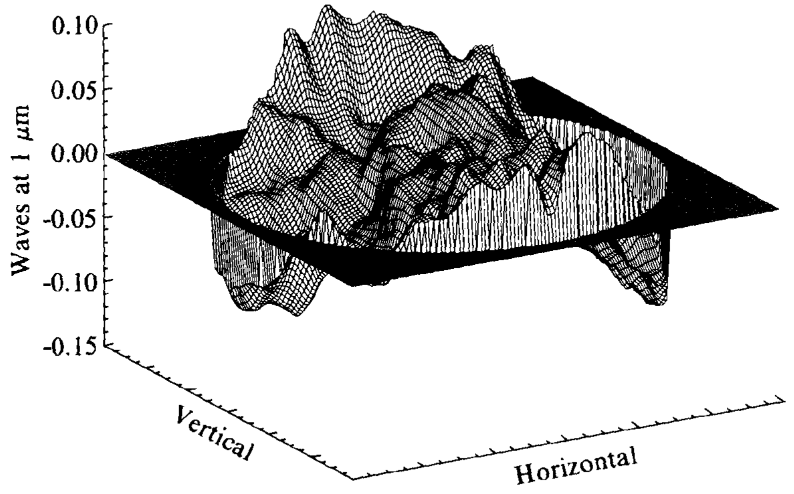

- Fabrication errors are correlated
- Spec: $\lambda/9$ at 0.6328-μm P-V

G2967

Fig. 44.30
Interferometrically measured wave front of four multisegmented amplifier (MSA) disks in series. Although these disks are slightly larger and slightly thicker than the 20-cm amplifier disks, they are indicative of what can be expected from the passive 20-cm amplifier.

The use of Pyrex®20 water jackets on the cerium-doped quartz flash lamps initially offered the opportunity to eliminate blast windows, thereby reducing costs. It was hypothesized that the Pyrex® UV-absorption edge, which covered the UV window in the cerium-doped quartz absorption at ~250 nm, would eliminate any UV light in the amplifier that molecular oxygen might absorb. Time-resolved interferometric measurements of the atmosphere above a flash-lamp array operated at the equivalent-energy level of the SSA revealed the existence of significant optical-path disturbances as shown in Fig. 44.31. Replacement of the atmosphere with pure N_2 did not affect the result. It is currently hypothesized that these disturbances are due to simple acoustic waves rather than UV absorption. This hypothesis is supported by the significant reduction of the effect when a blast window is reintroduced as shown in Fig. 44.32. The blast window should act as an acoustic-impedance mismatch, keeping most of the acoustic energy in the pump module. As a result of these measurements, the 20- and 15-cm disk amplifiers used on the OMEGA Upgrade will have blast windows.

Conclusion

The OMEGA Upgrade will use a 20-cm, single-aperture disk amplifier as the final amplifier. In keeping with LLE's direct-drive mission, special emphasis has been placed on understanding the amplifier's gain uniformity and wave-front quality before actual construction of hardware. Construction of the prototype amplifier will take place in the last quarter of 1990. Testing of the prototype will begin in the first quarter of 1991. Results of the testing will be reported in a future LLE Review article.

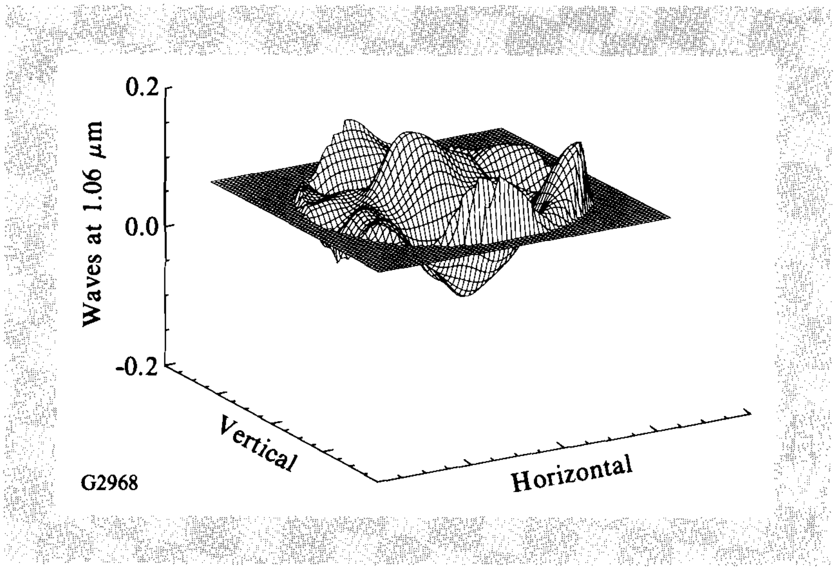

Fig. 44.31
The measured wave front above a 30-cm section of a flash-lamp array without a blast window. The bottom of the beam (closest to the array) is in the foreground.

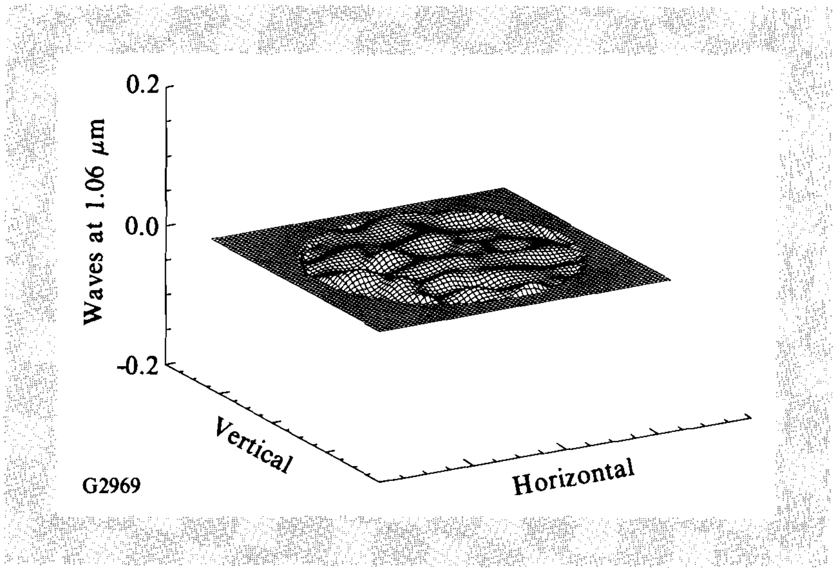

Fig. 44.32
The measured wave front above a 30-cm section of a flash-lamp array with a blast window. The bottom of the beam (closest to the array) is again in the foreground. The remaining wave front is comparable to that of the empty interferometer.

ACKNOWLEDGMENT

This work was supported by the U.S. Department of Energy Division of Inertial Fusion under agreement No. DE-FC03-85DP40200.

REFERENCES

1. LLE Review **41**, 4 (1989).
2. Laser Program Annual Report 1980, Lawrence Livermore National Laboratory, UCRL 50021-80 (1981), pp. 2-234–2-237.
3. Annual Report to the Laser Facility Committee (1985), Rutherford Appleton Laboratory, pp. A6.6–A6.12.

4. OMEGA Upgrade Preliminary Design Document, DOE/DP40200-101 (1989).
5. L. M. Frantz and J. S. Nodvik, *J. Appl. Phys.* **34,** 2346 (1963).
6. Laser Program Annual Report 1986, Lawrence Livermore National Laboratory, UCRL 50021-86 (1987), pp. 4-14–4-56.
7. Laser Program Annual Report 1987, Lawrence Livermore National Laboratory, UCRL 50021-87 (1989), pp. 3-48–3-88.
8. Laser Program Annual Report 1986, Lawrence Livermore National Laboratory, UCRL 50021-86 (1987), pp. 4-55–4-56.
9. Private communication with K. Moncur, KMS Fusion, Inc. (1989).
10. M. Zahn *et al.*, "Dielectric Properties of Water and Water/Ethylene Glycol Mixtures for Use in Pulsed Power System Design," in *Proceedings of the IEEE,* Vol. 74, No. 9 (1986).
11. Laser Program Annual Report 1985, Lawrence Livermore National Laboratory, UCRL 50021-85 (1986), pp. 7-18–7-25.
12. Laser Program Annual Report 1986, Lawrence Livermore National Laboratory, UCRL 50021-86 (1987), pp. 7-142–7-146.
13. The code used is a greatly updated and enhanced version of the code ZAP originally written by Systems, Science and Software for the Naval Research Lab by J. H. Alexander, M. Troost, and J. E. Welch, ARPA order number 660, Contract number N00014-70-C-0341 (1971).
14. M. S. Mangir and D. A. Rockwell, *IEEE J. Quantum Electron.* **QE-22,** 574 (1986).
15. J. E. Murray, H. T. Powell, and B. W. Woods, UCRL-93321 (1986), p. 13.
16. J. Eggleston, Ph.D. thesis, Stanford University, 1982, pp. 16–17. Available from University Microfilms Inc., Ann Arbor, MI.
17. B. A. Boley and J. H. Weiner, *The Theory of Thermal Stresses* (Wiley, New York, 1960), pp. 109–116.
18. Laser Program Annual Report 1982, Lawrence Livermore National Laboratory, UCRL 50021-82 (1983), p. 7–74.
19. Interferometric data supplied by D. Pileri of the Special Optics Fabrication Group, Eastman Kodak Co., Rochester, NY.
20. Pyrex® is a product of Corning Glass Works, Corning, NY.

Section 2
ADVANCED TECHNOLOGY DEVELOPMENTS

2.A Development of Optical Coatings for the OMEGA Upgrade

An intensive in-house effort in the past year has produced coatings and devices that will survive the peak 351-nm fluence expected in the OMEGA Upgrade. The stringent ultraviolet requirements for the upgrade stem from the decision to place the frequency-conversion crystals in the laser bay (rather than at the target chamber).[1] At that time, only one report of satisfactory laser-damage thresholds for 351-nm high reflectors existed.[2] Reports of satisfactory distributed phase plates (DPP's) did not exist, and tests indicated the thresholds of existing designs would not suffice. Modification of the laser beam-transport-system design (see Section 1.A, this issue) lowered the thresholds from those listed in the Preliminary Design Document.[1] These new thresholds are listed in Table 44.III. As seen in the table, fluences in the blue were lowered for high reflectors and DPP's, but remained the same for antireflection coatings.

The pending need for upgrade coatings dictated the development of improved coating technologies. Since we investigated variations on established methods, issues other than damage, such as scale-up to large apertures, optical performance, and environmental performance, are assumed to be known and previously addressed by the optical community. Optical coating of high reflectors by evaporation is the most common technique used for high-energy lasers. We report on coatings using standard evaporation methods and on those using an ion-assisted deposition (IAD) technique. Sol-gel deposition methods are the preference for antireflection coating.

Table 44.III: Previous and current maximum fluence levels for the OMEGA Upgrade 351-nm components (main pulse, 0.6 ns).

	Previous (Preliminary Design Document)	Current Design	Process
Frequency-conversion crystals	3.8 J/cm^2	3.8 J/cm^2	Sol-gel
Relay lenses	3.8 J/cm^2	3.8 J/cm^2	Sol-gel
Transport mirrors	3.8 J/cm^2	2.9 J/cm^2	Dielectric evaporation
Refocusing asphere	3.6 J/cm^2	2.9 J/cm^2	Sol-gel
Distributed phase plate	3.6 J/cm^2	3.6 J/cm^2	Ion etch/sol-gel

G3014

Development of a sol-gel coating capability and related damage-test results are reported for various substrates. Finally, development of an etching technique for DPP's that can handle substantially higher fluences than previous designs is described.

Development Procedure

The study began by choosing materials and process variables that gave favorable results in the past, then depositing and damage testing the coating. Favorable results were explored further. Generally, no attempt was made to further characterize the coating or understand the reason for the performance. While this approach is not scientifically satisfying, it is a very effective development method when the in-house coating and damage test groups can closely collaborate. Also, since there is no well-established set of precursors to laser damage, testing remains the only reliable measure of the reliability of a coating in a large laser system.

Coatings were deposited on well-characterized, 5-cm-diam substrates of either BK-7, Pyrex®, or fused silica. Each substrate was cleaned using equipment and procedures established for cleaning the large substrates used on OMEGA. The aqueous process uses a series of mechanical scrubs, rinses, and soaks in ultrasonic baths. The final rinse with 18-MΩ water takes place in a class-10 clean-room environment where the substrate is left to dry. The 54-in. and 28-in. deposition chambers used for this study were both equipped with electron-beam evaporation sources for reactive-gas (oxygen) evaporation. With the exception of some of the ion-assisted coatings, all substrates were held at 200°C during deposition. This is based upon in-house experience and an extensive parameter study with tantalum pentoxide,[3] which gave the best damage results for low substrate temperatures. These low temperatures also reduce the possibility of coating fracture. The other deposition parameters were adjusted to give low average absorption for thin films in the 300- to 400-nm range.

All coatings were tested in the LLE damage test facility with 351-nm, 0.7-ns FWHM pulses. Both 1-on-1 and N-on-1 testing were performed on the samples. In 1-on-1 testing (see Fig. 44.33), a new site is chosen for each laser shot. A minimum of ten sites are usually examined. The 1-on-1 damage threshold is defined as the average of the highest nondamaging fluence and the lowest damaging fluence seen in all sites. In N-on-1 testing, one site is subjected to successive laser pulses, each one increasing in fluence above the previous pulse until damage is observed. Three to ten sites are tested in this manner, and the fluences at which damage occurs are averaged to give the N-on-1 damage threshold. N-on-1 testing is more typical of the operation of a large laser facility, demonstrating a hardening effect in the tested surface.[4] Damage is assumed to have occurred whenever a new scatter site appears within a 100 × 100-μm area observed under dark-field incandescent illumination.

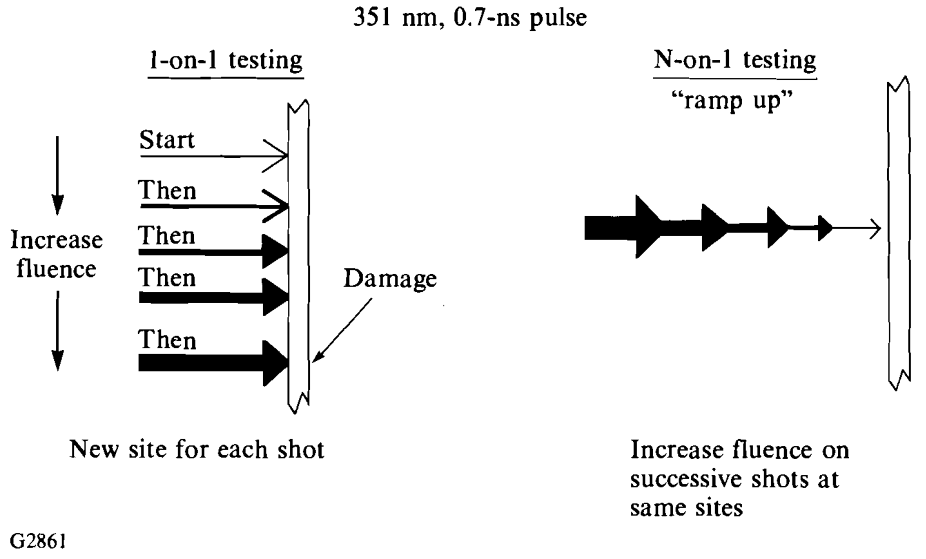

Fig. 44.33
In 1-on-1 testing (left) a site is subjected to laser radiation, examined, then the process is repeated at a higher fluence on a new site until damage is observed on several sites. In N-on-1 testing (right), the fluence is gradually increased at a single site. Between each laser pulse, the surface is examined for damage.

High Reflectors for 351 nm

Two pieces of equipment were used to produce high-reflector coatings: a 54-in.-wide chamber with a planetary-substrate rotation (for high uniformity on large substrates) and a 28-in.-wide system with a single-substrate rotation. The two chambers allowed for two different approaches to achieve high damage thresholds; a materials/design survey was conducted in the larger coater, while the smaller coater concentrated on one pair of materials under different process conditions. The effects of oxygen-ion assist were primarily investigated in the smaller chamber with the best results later repeated in the larger chamber. Typical deposition parameters for some materials are given in Table 44.IV. The results from the materials/design survey are reported first.

Table 44.IV: Deposition parameters for various high-reflector coating materials—200°C substrate temperature.

Material	Deposition Rate Å/s	O_2 Backpressure (Mbar)
SiO_2	5	4×10^{-5}
MgF_2	5	none
Y_2O_3	2	1.2×10^{-4}
Sc_2O_3	1.5	1.7×10^{-4}
ZrO_2	2	1.3×10^{-4}
HfO_2	0.5	1.7×10^{-4}
Ta_2O_5	1–2	1.8×10^{-4}

G3015

Laser-damage thresholds (LDT) of single layers of materials do not correlate well with thresholds of those same materials in multilayer designs.[5] Therefore, we tested only high-reflector designs, choosing materials that had shown potential for high LDT at 351 nm in other studies. All of the coatings were made to meet component specification for the OMEGA Upgrade; blue reflectors were designed to have reflectivity greater than 0.995 for both polarizations at the given incidence angle. Thus, while the coatings may physically differ in the number of layers, they all are functionally equivalent.

The N-on-1 results of the first set of coatings are shown in Fig. 44.34. The threshold is identified by the circle or triangle, and the error bars represent one standard deviation for the measurements on each sample. Yttria/silica designs were considered because they can be stripped from a surface without repolishing.[6] Despite considerable effort, these coatings never achieved acceptable thresholds. Scandia and zirconia-based coatings performed well, as they had in other studies,[2] with scandia/silica coatings

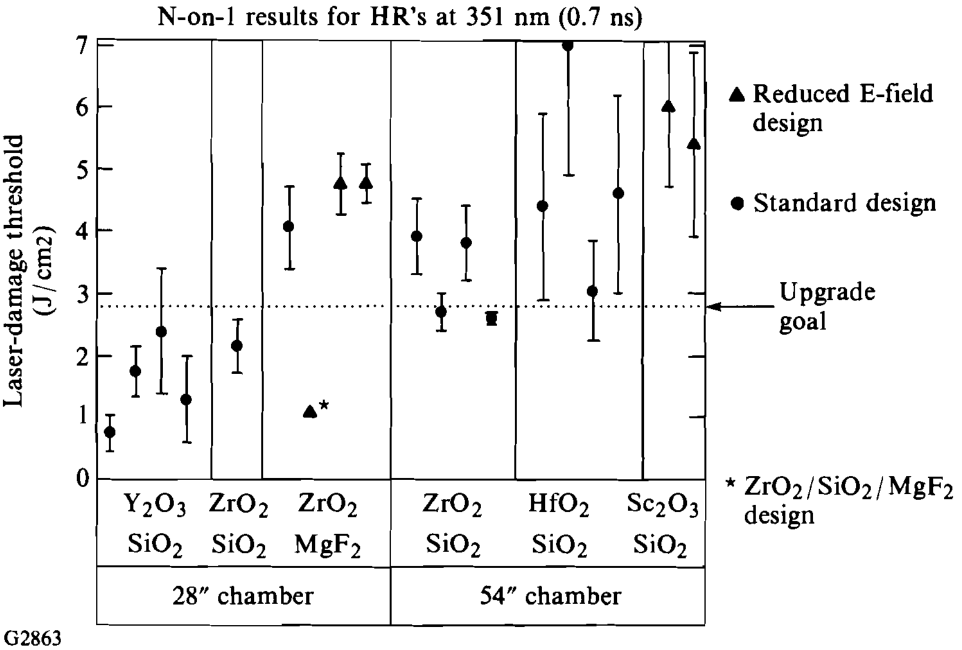

Fig. 44.34
N-on-1 laser damage test (LDT) results for a materials study with evaporated coatings in two different chambers. The design requirement for the OMEGA Upgrade is indicated by the dotted line. The error bars show a one-standard deviation of the data from the mean.

exceeding the upgrade goal considerably. There are several noteworthy results in this data: (1) hafnia/silica coatings performed very well contrary to previous results[2]; (2) zirconia/magnesium fluoride coatings also had high thresholds except for a hybrid material design; (3) the best results came from designs with reduced electric field in the outer four layers; and (4) the data suggest that coatings made in the larger chamber have higher thresholds. The difference seen between the chambers may be attributed to variations in process parameters for the two systems.

Design variations using reduced E-fields and starting materials were investigated for the promising hafnia/silica combination in the 54-in. chamber. Reduced E-field designs of high reflectors[7] have exhibited higher damage thresholds in other studies.[2] In these designs, the time-averaged electric-field intensity is reduced in the most damage-prone material, which is hafnia in the current coatings. The peak electric-field intensity is also moved from the interface into the low-index layer where the damage resistance may be greater. Our data, seen in Fig. 44.35, tends to agree with these premises. The highest thresholds in this study were consistently produced by reduced E-field designs.

At the time of this study, one vendor[8] supplied two grades of hafnia (standard grade and UV grade). Spectrographic analysis showed the UV grade had significantly less titanium and zirconium contamination and less trace contaminants. Despite the lower contamination, Fig. 44.35 shows that for a standard high-reflector (HR) design there was actually a slight decrease in the threshold for the more pure hafnia, while no perceived difference was observed for the reduced E-field designs between the two materials. This was an intriguing result since spectroscopy confirmed that the UV-grade hafnia did have a lower absorption edge, which typically corresponds to a higher laser-damage threshold.

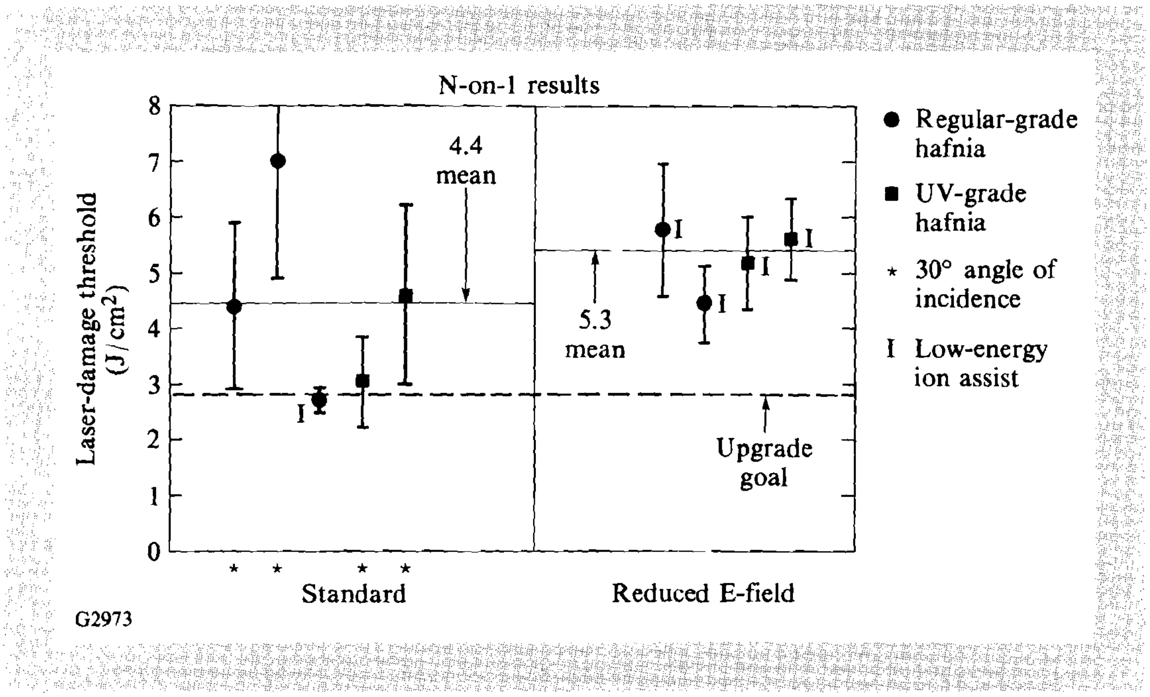

Fig. 44.35
Laser damage test (LDT) results for hafnia-silica high reflectors. The combination of a reduced E-field design and ion assist produced the most consistent results in this study.

Coatings using magnesium fluoride as the low-index material were made with zirconia or hafnia as the high-index material. The zirconia coatings produce the highest thresholds for any HR made in the smaller chamber (Fig. 44.36). Oddly, the same coating made in the larger chamber performed poorly. The standard design with hafnia (UV grade) and magnesium fluoride also performed poorly at about 3 J/cm^2. The same materials in a reduced E-field design almost doubled in damage threshold (5.4 J/cm^2). The small error bar suggests that HfO_2/MgF_2 coatings may perform better than ScO_2/SiO_2 coatings on a laser system. These results show the magnesium-fluoride-based HR coatings are likely candidates for upgrade transport optics, but they require further study and process development.

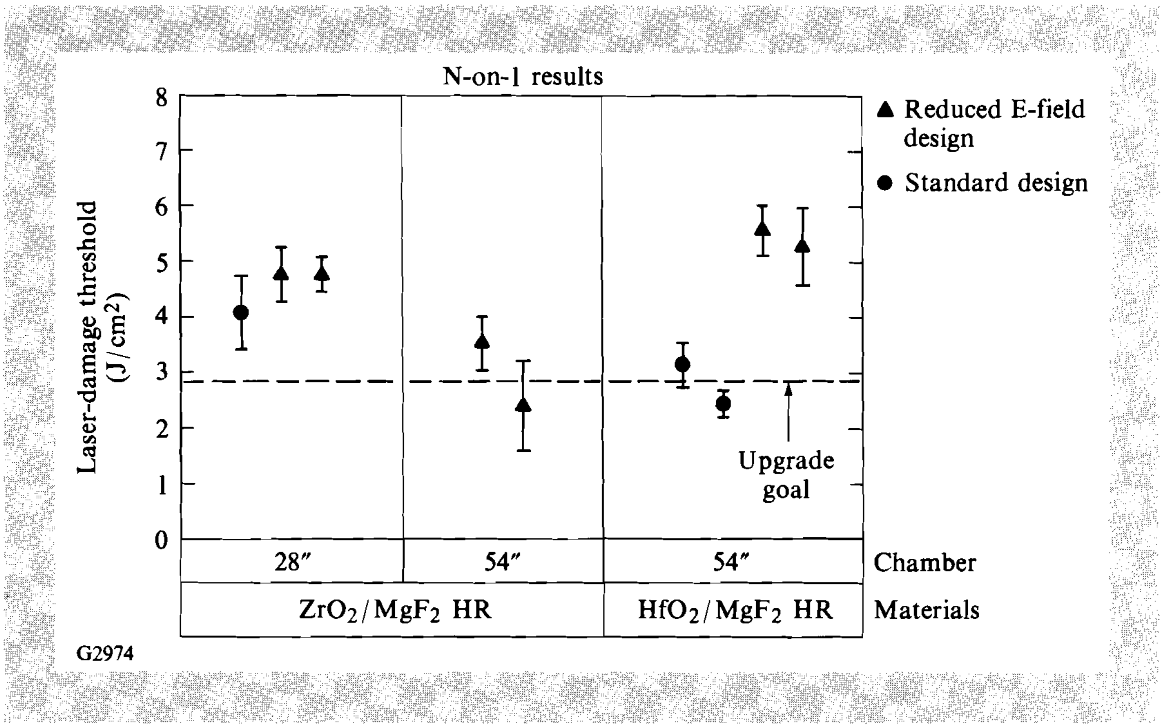

Fig. 44.36
Coatings produced with MgF_2 for the low-index layer show significant variation in LDT. Both ZrO_2/MgF_2 and HfO_2/MgF_2 high reflectors show promise for use at OMEGA Upgrade fluence levels.

Special emphasis was placed on the use of scandium oxide since a significant amount of promising damage data has been obtained with this material. However, the cost of the material is so high that its use would be prohibitively expensive for the OMEGA Upgrade. In an attempt to reduce the cost of scandia coatings but still retain the best qualities of the material, we tested several hybrid designs. These consisted of a multilayer next to the substrate consisting of HfO_2/SiO_2 (15 layers), followed by a 10-layer stack of a Sc_2O_3/SiO_2 multilayer. The damage-test results for a standard design and a reduced E-field design are seen in Fig. 44.37. Results for the same reactive-evaporation (RE) design, but with MgF_2 substituted for the silica, are also given. The thresholds are unimpressive for most of these coatings with few exceeding the upgrade requirement. The unusually small error bar implies a distinct onset of damage, which may indicate a damage mechanism different from that in two-material HR's. Physical properties such as stress, hardness, and adhesion between layers are all probable causes for coating failure. It is possible the multiple material combinations exacerbate these problems.

Most of the tested coatings meet OMEGA Upgrade optical and mechanical requirements. Some of the coatings made with magnesium fluoride are softer and scratch more easily, but survive well in a benign laboratory environment. Multilayers made with low-voltage ion assist are the hardest coatings. The most promising coatings are the hafnia/magnesium fluoride

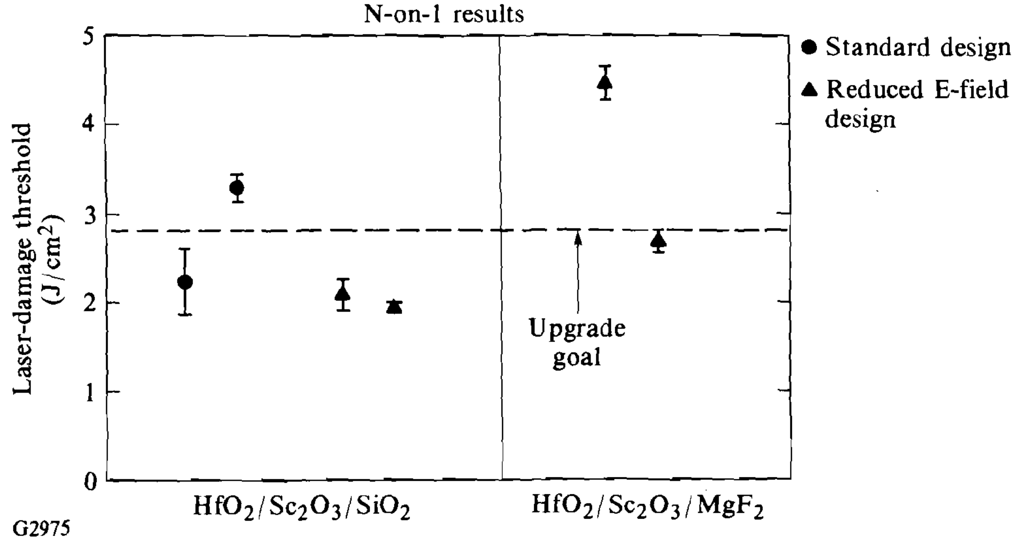

Fig. 44.37
The LDT of hybrid high reflectors using scandia as an upper-stack component. Although scandia generally provides a promising LDT in HR coatings, its performance in the hybrid-HR designs was disappointing.

and hafnia/silica coatings. Future work will gather data for non-normal incidence-angle coatings for both hafnia designs and some zirconia designs. More data will be gathered to document differences in thresholds due to equipment used and method of operation.

Ion Assist of High Reflectors

Ion-assisted deposition (IAD) is a combination of evaporation and ion beam-sputtering techniques. In a standard evaporation geometry (see Ref. 9) with an electron-beam source, ions from a broad-beam source[10] are directed toward the substrate. The ions with a kinetic energy about 100 times higher than the evaporant ions can effect chemical and physical changes in the films. Resultant coatings have significantly altered structures, reduced void fractions, less roughness, and less absorption. To investigate the effect of ion assist on the damage threshold of HR coatings we used low-energy (200-eV) oxygen ions. Structural changes to the film were kept to a minimum by maintaining low ion-beam currents.

Early tests with IAD coatings consistently gave poor damage results. Since average absorption in these films was measurably reduced, local contamination from the ion source was suspected of lowering the thresholds. The ion source consists of a discharge chamber with a tungsten filament, accelerator grids composed of graphite, and another tungsten filament for beam charge neutralization. To test for contamination, we ran the gun without using the accelerator grids (just the filaments on, producing negligible grid erosion), and then with two levels of accelerator-grid erosion. The results for a zirconia/silica HR made in the 28-in. chamber are given in Fig. 44.38(a). A slight improvement in the damage threshold is seen for both the negligible- and low-erosion cases, while a steep drop in threshold was observed when the grid erosion was high. A final coating was made with a different gun equipped with molybdenum grids with settings to give low erosion. This coating gave the highest threshold for this material pair seen in the 28-in. chamber.

The experiments with IAD were continued at this point on the larger, 54-in. chamber with the molybdenum grid ion source. This chamber is equipped with a planetary-substrate rotation causing intermittent ion bombardment at the substrate level. The peak ion-beam flux impinging on the substrate was similar to the continuous flux measured in the smaller, 28-in. chamber. Coatings with both negligible erosion and low-erosion IAD of ZrO_2/SiO_2 layers were found to have thresholds similar to conventionally deposited substrates [Fig. 44.38(b)]. A coating made with IAD of only the ZrO_2 layers had a slightly higher damage threshold than all other tested zirconia/silica coatings. These near-optimum IAD conditions were used to make the hafnia/silica reflectors already described in Fig. 44.35. While the superior damage performance of the hafnia coatings cannot be solely attributed to IAD, it is clear that no detrimental effects from IAD were observed.

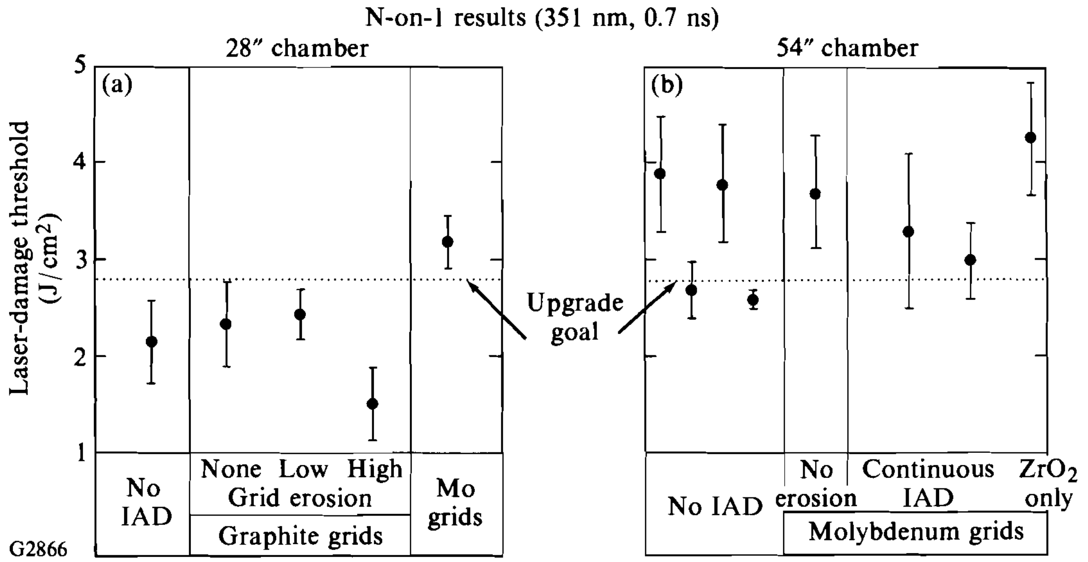

Fig. 44.38
LDT results for ZrO_2/SiO_2 coatings under various conditions of ion assist. Fig. 44.38(a) shows that contamination from graphite grids in the ion source was probably responsible for lower thresholds. Coatings made with molybdenum grids showed the highest threshold for these materials in the 28-in. chamber. Figure 44.38(b) shows little change for the ZrO_2/SiO_2 HR when the ion source is operated continuously. However, operating the source during only the high-index ZrO_2 layer results in a higher threshold.

The use of IAD adds a large number of parameters to the deposition process, including ion-source design, electrical settings, and gas choice. By making reasonable choices for these parameters, guided by past experience with IAD-modified films and laser damage, we have made better films in terms of both damage resistance and mechanical properties. These films were made in a production-sized coater under intermittent bombardment. While scale-up of all properties still must be demonstrated, we believe this will be a straightforward extension of current technology.

Sol-Gel Coatings

Early tests of dielectric coatings made with physical vapor-deposition methods for OMEGA Upgrade applications were disappointing (Fig. 44.39). Coatings using conventional, IAD, or reactive-ion plating (RIPD)[11] did not meet threshold goals for the upgrade. Sol-gel coatings[12] have been shown to meet both damage and optical requirements of laser systems similar to the OMEGA Upgrade. We tested several coatings supplied by Lawrence Livermore National Laboratory (LLNL) and Rutherford labs in England. All coatings had fairly good thresholds with two easily exceeding upgrade damage goals. A polymeric vapor-penetration barrier coat over one of the Rutherford samples (labeled COLSI/OC) drastically reduced the threshold.

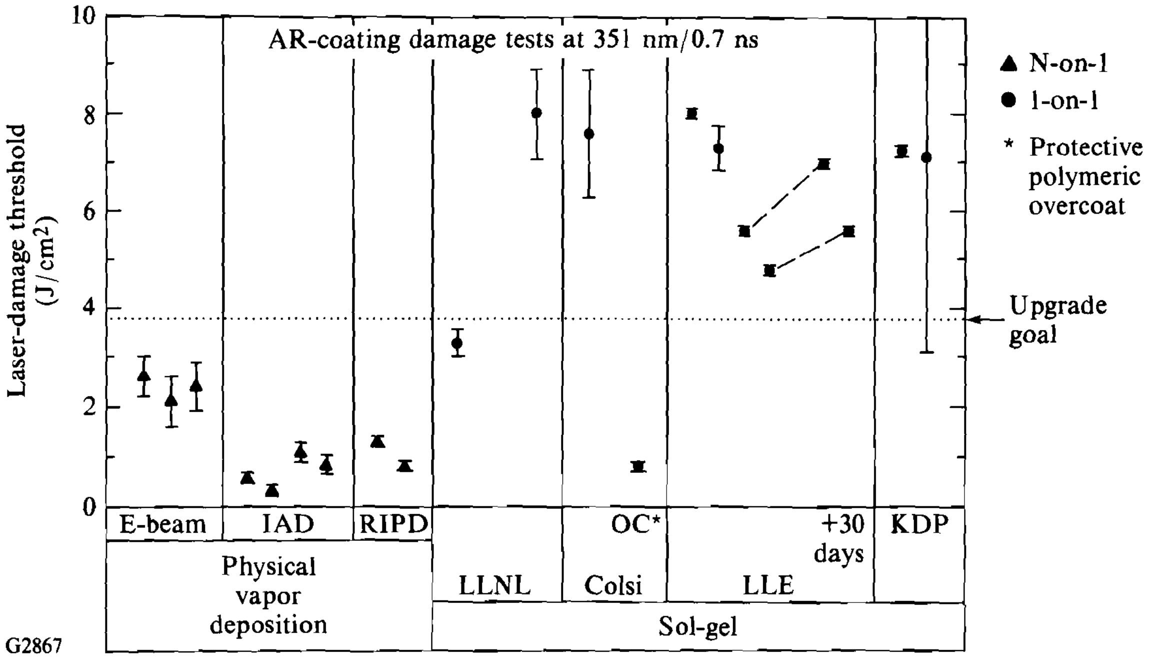

Fig. 44.39
LDT results of AR coating produced both by physical vapor-deposition techniques and sol-gel methods. Some of the sol-gel coatings were tested after a period in a laboratory environment. No degradation was observed in these coatings. All coatings were applied to silica substrates with the exception of the potassium di-hydrogen phosphate (KDP).

We developed a capacity to produce and purify the sol-gel solution, and spin a controlled thickness onto damage-test substrates. Coatings were applied to fused silica cleaned by the same aqueous method described for high reflectors. The coatings were spun in a class-100 clean room. Several pieces of potassium di-hydrogen phosphate (KDP) were also cleaned (using non-aqueous solvents) and sol-gel coated. The damage results for these samples (Fig. 44.39) show that most of these coatings tested well above OMEGA Upgrade requirements. Two samples were retested after standing exposed for 30 days in a typical laboratory environment. Neither coating exhibited deleterious effects after aging.

Sol-gel development has continued with the emphasis on scale-up problems. A dip-tank arrangement has been assembled and successfully tested with substrates up to 30 cm in size. Small prototype tooling has been designed and tested for two-sided spin coating of substrates. Also, work is proceeding on design of full-size spinner tooling. Prototypes of bonded KDP crystals for the OMEGA Upgrade will be coated. To date, the bonding material integral to the design of the frequency-conversion crystals (FCC) has been analyzed and may prove to be a contamination problem for the sol-gel coating. Further development is required in this area.

Distributed Phase Plates

The existing distributed phase plates (DPP's) for the OMEGA laser were made by evaporating the phase-retardation pixels onto a flat optic through a patterned photoresist coating.[13] These devices were adequate for current OMEGA peak fluences and had the advantage that the underlying antireflection and DPP coating could be removed. This process did not meet OMEGA Upgrade damage requirements as seen in Fig. 44.40. Damage tests were conducted on a patterned and unpatterned optic coated with an evaporated silica retardation layer. The antireflection coating was omitted to improve the damage characteristics of the device. All of these devices failed to exceed the damage criteria for the upgrade.

The new method for fabricating DPP's involves etching the pattern into the silica substrate. The threshold of these etched devices should be higher since there is no possibility of trapping contaminants within or underneath an evaporated layer. Unless the substrate surface is damaged during the etching process, a threshold comparable to that of an uncoated fused-silica surface will be attained. The patterns were etched into photoresist-patterned substrates using the same ion sources as described in the section on IAD. The working gas for etching was argon, which assured a longer filament life for the ion sources. The substrates were rotated during deposition, and the ion source was pointed off center, which reduces the etch rate but provides for better uniformity across the plate. After etching, the photoresist is removed with a solvent, and the surface is cleaned. Both a sol-gel AR-coated and an uncoated etched DPP were laser-damage tested. Test sites included both the "on" and the "off" hexagons in the array. The thresholds (Fig. 44.40) are among the highest we have tested for any surface at 351 nm, 0.7 ns. The tests were limited by the failure of the index-

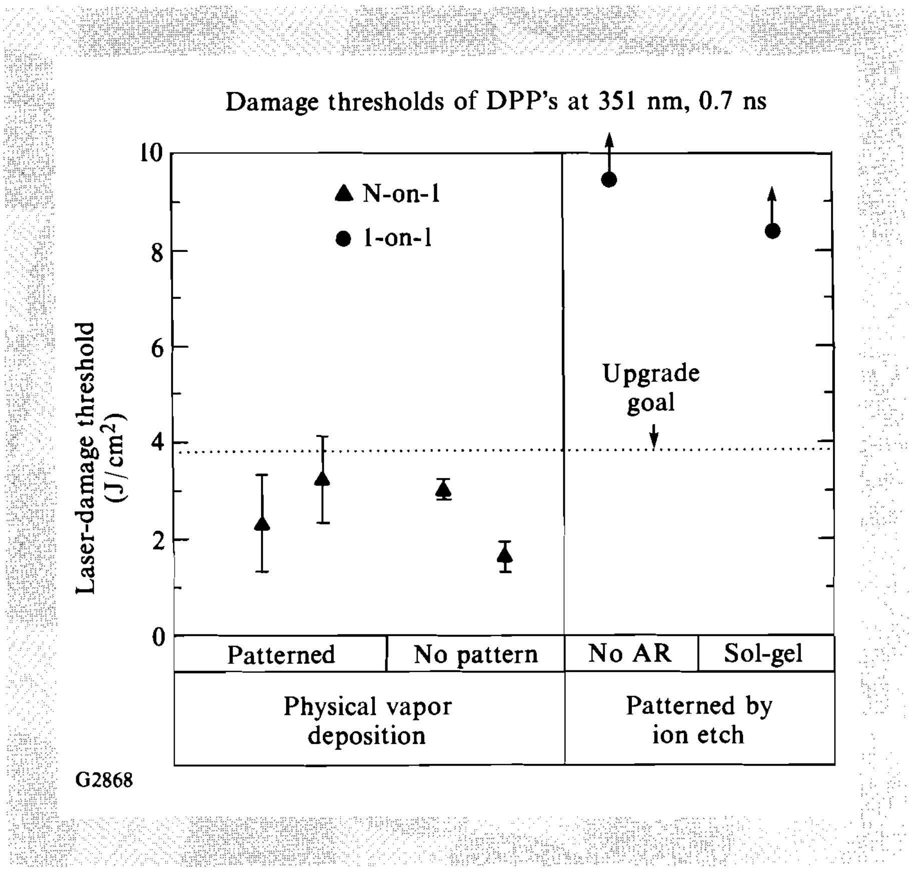

Fig. 44.40
The thresholds of the distributed phase plates (DPP's) (left) are well below the required level, even in the ideal case of a SiO_2 layer directly deposited onto a silica substrate without a pattern. Conversely, the thresholds of the etched DPP's approach those of polished uncoated surfaces.

matching fluid for the rear surface of the optic, so only a lower bound on the threshold is available. The pixel edge structure is also an improvement over the old DPP's. The magnified edges of both the etched and evaporated DPP may be seen in Fig. 44.41. The smoother, well-defined edges of the etched DPP will reduce scatter and also reduce the effect of size mismatch between the on and the off pixels. There was no effect on the phase difference when the sol-gel AR was applied to the DPP.

Future work on DPP's will focus on scale-up and etch-thickness control of the ion-etched DPP's. Up to now, damage-test pieces were created with a small, 3-cm ion source in a bell-jar vacuum system. Existing focused and defocused 8-cm ion sources will be characterized, modeled, and optimized for the best geometry for high uniformity across a clear aperture of 30 cm. The sources will be installed in existing chambers for uniformity testing and etch-rate measurement. A monitoring system will be developed for unattended automatic etching of the DPP. Photoresist coating and processing technology will also be developed for the upgrade apertures.

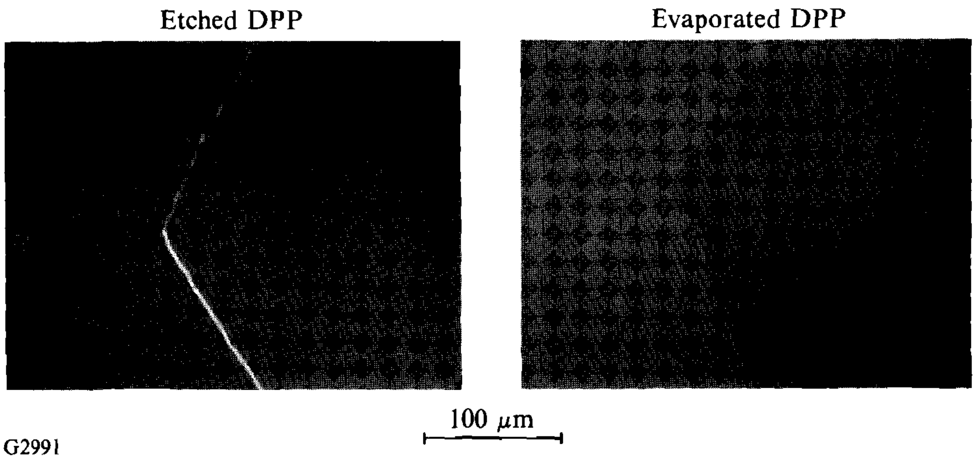

Fig. 44.41
Etched DPP's have better edge definition (left) than DPP's made with the deposition process. Higher edge definition produces less scatter, especially in smaller DPP patterns.

Conclusions and Further Study

Small-scale prototypes of all 351-nm components have been fabricated and have laser-damage thresholds exceeding the design requirements of the OMEGA Upgrade. Further testing and coating will provide better statistics for reflectors at both normal and high-incidence angles. Other considerations of scale-up such as scatter, stress, coating endurance, and damage properties of large aperture coatings will be explored. Development of sol-gel coating will continue with emphasis on the problems in coating the top-hat design of the KDP frequency-conversion crystals, large focusing aspheres, and blast windows and water jackets for the single-segmented disk amplifiers. Finally a significant effort will go into scaling the etched-DPP technology to OMEGA Upgrade-sized apertures.

ACKNOWLEDGMENT

This work was supported by the U.S. Department of Energy Division of Inertial Fusion under agreement No. DE-FC03-85DP40200 and by the Laser Fusion Feasibility Project at the Laboratory for Laser Energetics, which has the following sponsors: Empire State Electric Energy Research Corporation, New York State Energy Research and Development Authority, Ontario Hydro, and the University of Rochester.

REFERENCES

1. OMEGA Upgrade Preliminary Design Document, DOE/DP40200-101 (1989).
2. C. K. Carniglia, T. Tuttle-Hart, F. Rainer, and M. C. Staggs, *Nat. Bur. Stand. Spec. Publ. 688,* Laser Induced Damage to Optical Materials: 1983, pp. 347–353.
3. D. Milam *et al., Appl. Opt.* **21,** 3689 (1982).

4. LLE Review **20,** 175 (1984).
5. W. H. Lowdermilk and D. Milam, "Review of Ultraviolet Damage Threshold Measurements at Lawrence Livermore National Laboratory" (SPIE, Bellingham, WA, 1984), Vol. 476, p. 143.
6. D. J. Smith, C. J. Hayden, B. U. Krakauer, A. W. Schmid, and M. J. Guardalben, *Nat. Bur. Stand. Spec. Publ. 746,* Laser Induced Damage in Optical Materials: 1985, 284 (1988).
7. J. H. Apfel, *Appl. Opt.* **16,** 1880 (1977).
8. EM Industries, Hawthorne, NY.
9. LLE Review **43**, 149 (1990).
10. H. R. Kaufman, J. J. Cuomo, and J. M. E. Harper, *J. Vac. Sci. Technol.* **21,** 725 (1982).
11. Balzers High Vacuum, Hudson, NH.
12. I. M. Thomas, *Appl. Opt.* **25,** 1481 (1986).
13. LLE Review **33,** 1 (1987).

Section 3

NATIONAL LASER USERS FACILITY NEWS

During the fourth quarter of FY90 **A. Honig** (Syracuse University) and **H. Griem** (University of Maryland) used the OMEGA laser facility for NLUF experiments.

A. Honig and his group are testing the cold-entry target-handling system Honig has been developing for his spin-polarized D_2 experiments. This system should prove to be useful for high initial density gas-filled plastic-shell targets as well as cryogenic-fuel targets. Initial problems have been solved and a target was centered in the OMEGA target chamber during the group's last visit to LLE.

J. Moreno from H. Griem's group used a McPigs spectrograph to measure the time dependence of XUV emission from multilayer targets. The targets were fabricated at LLE for these experiments and included both solid glass spheres and glass shells with layers of plastic and metals. The spectral signature of the metal layers was measured as a function of the plastic-layer thickness.

ACKNOWLEDGMENT

This work was supported by the U.S. Department of Energy Division of Inertial Fusion under agreement No. DE-FC03-85DP40200.

Section 4
LASER SYSTEM REPORT

4.A GDL Facility Report

In the first half of the fourth quarter of FY90, GDL was dedicated to only three user efforts: the x-ray laser experiments, the University of Illinois experiments, and the OMEGA Upgrade development studies. The x-ray laser shots were the last of a series devoted to resonantly photo-pumped x-ray lasers. **G. Banas** from the University of Illinois, in collaboration with **H. E. Elsayed-Ali** (LLE), performed NLUF experiments on laser hardening of materials. The upgrade development was the study of a prototype frequency-conversion crystal (FCC) that will be used in the OMEGA Upgrade. In the second half of the quarter, GDL was devoted (excluding laser shots) to the development of pulse-shaping technology, which will ultimately be used on OMEGA.

A summary of GDL operation this quarter follows:

Beamline Test, Calibration, Tuning, and Laser Alignment Shots	66
Target Shots	
X-Ray Laser	19
NLUF User	43
OMEGA Upgrade FCC Tests	47
TOTAL	175

ACKNOWLEDGMENT

This work was supported by the U.S. Department of Energy Division of Inertial Fusion under agreement No. DE-FC03-85DP40200 and by the Laser Fusion Feasibility Project at the Laboratory for Laser Energetics, which has the following sponsors: Empire State Electric Energy Research Corporation, New York State Energy Research and Development Authority, Ontario Hydro, and the University of Rochester.

4.B OMEGA Facility Report

The OMEGA oscillator was converted to 50-MHz operation during the fourth quarter of FY90. This conversion enables it to be synchronized to either the GDL oscillator or the probe-beam oscillator. The conversion also incorporates an oscillator that is well baffled and shielded from air currents and has proved to be more stable than the previous 66-MHz oscillator.

Progress was made on the new temporal fiducial beam used to provide a timing reference for the OMEGA target diagnostics. This fiducial uses a 16-mm amplifier after the oscillator as a three-pass regenerative amplifier. The output of the amplifier is converted to the fourth harmonic of YLF and is then transported to the OMEGA target chamber. This fiducial is being optimized and readied for injection into the fiber-optic bundle coupled to the streak cameras on the target chamber.

Target shots were undertaken in support of laser-plasma interaction experiments, gas-filled plastic-shell implosion experiments, and surrogate-cryogenic-shell implosion experiments. The OMEGA system had to be converted from a spherical-target facility to a flat-target facility for the laser-plasma interaction experiments. This required setting up the optics to redirect one of the OMEGA beams to act as an interaction beam, retiming of several OMEGA beams to optimize the formation of the plasma needed for the measurement, and synchronization of the OMEGA oscillator with the probe-beam oscillator. Both the gas-filled plastic shells and the CD (cryogenic surrogate) shell targets are in support of the ongoing yield/density programs.

A shot summary for the OMEGA laser this quarter is as follows:

Driver Line	90
Laser Test	72
Target	202
Software	9
TOTAL	373

ACKNOWLEDGMENT

This work was supported by the U.S. Department of Energy Division of Inertial Fusion under agreement No. DE-FC03-85DP40200 and by the Laser Fusion Feasibility Project at the Laboratory for Laser Energetics, which has the following sponsors: Empire State Electric Energy Research Corporation, New York State Energy Research and Development Authority, Ontario Hydro, and the University of Rochester.

PUBLICATIONS AND CONFERENCE PRESENTATIONS

Publications

H. E. Elsayed-Ali and J. W. Herman, "Picosecond Transient Surface Temperature Measurement by Reflection High-Energy Electron Diffraction," *Ultrafast Phenomena VII,* edited by C. B. Harris, E. Ippen, G. A. Mourou, and A. H. Zewail (Springer-Verlag, Berlin, 1990), Vol. 53, pp. 371–373.

H. E. Elsayed-Ali, T. Juhasz, G. O. Smith, and W. E. Bron, "Femtosecond Thermomodulation of Single-Crystalline and Polycrystalline Gold Films," *Ultrafast Phenomena VII,* edited by C. B. Harris, E. Ippen, G. A. Mourou, and A. H. Zewail (Springer-Verlag, Berlin, 1990), Vol. 53, pp. 315–317.

R. Epstein and S. Skupsky, "Anticipated Improvement in Laser Beam Uniformity Using Distributed Phase Plates with Quasirandom Patterns," *J. Appl. Phys.* **68,** 924–931 (1990).

R. Q. Gram, M. D. Wittman, C. Immesoete, H. Kim, R. S. Craxton, N. Sampat, S. Swales, G. Pien, J. M. Soures, and H. Kong, "Uniform Liquid-Fuel Layer Produced in a Cryogenic Inertial Fusion Target by a Time-Dependent Thermal Gradient," *J. Vac. Sci. Technol. A* **8,** 3319 (1990).

H. L. Helfer, "Of Martian Atmospheres, Oceans, and Fossils," *Icarus* **87,** 228–235 (1990).

C. Immesoete, S. Scarantino, H. Kim, and L. Forsley, "Computer-Assisted Microballoon Selection for Inertial Confinement Fusion Targets," *J. Vac. Sci. Technol. A* **8,** 3324–3326 (1990).

J.-C. Lee, S. D. Jacobs, T. Gunderman, A. Schmid, T. J. Kessler, and M. D. Skeldon, "TEM$_{00}$-Mode and Single-Longitudinal-Mode Laser Operation with a Cholesteric Liquid-Crystal Laser End Mirror," *Opt. Lett.* **15,** 959–961 (1990).

G. G. Luther and C. J. McKinstrie, "Transverse Modulational Instability of Collinear Waves," *J. Opt. Soc. Am. B* **7,** 1125–1141 (1990).

B. Yaakobi, T. Boehly, and P. Audebert, "Focusing X-Ray Spectrograph for Laser Fusion Studies," *Rev. Sci. Instrum.* **61,** 1915–1919 (1990).

B. Yaakobi, D. K. Bradley, F. J. Marshall, J. P. Knauer, J. M. Soures, and C. P. Verdon, "Absorption Lines Analysis of Laser Imploded Targets," *Opt. Commun.* **77,** 167–173 (1990).

Forthcoming Publications

S. H. Batha, D. D. Meyerhofer, A. Simon, and R. P. Drake, "Enhanced Scattering from Laser-Plasma Interactions," to be published in *Physics of Fluids*.

T. Boehly, R. S. Craxton, R. Epstein, M. Russotto, and B. Yaakobi, "X-Ray Lasing in Thick Foil Irradiation Geometry," to be published in *Optics Communications*.

T. Boehly, M. Russotto, R. S. Craxton, R. Epstein, B. Yaakobi, L. B. DaSilva, J. Nilsen, E. A. Chandler, D. J. Fields, B. J. MacGowan, D. L. Matthews, J. H. Scofield, and G. Shimkaveg, "Demonstration of a Narrow Divergence X-Ray Laser in Neon-Like Titanium," to be published in *Physical Review A*.

S. H. Chen and M. L. Tsai, "New Thermotropic Chiral Nematic Copolymers Using (1S, 2S, 3S, 5R)-(+)- and (1R, 2R, 3R, 5S)-(-)-Isopinocampheol as Building Blocks," to be published in *Macromolecules*.

H. C. Chen, G. Mourou, and R. Knox, "Time-Resolved Electron Diffraction from Pulse-Excited Crystalline Gold Films," to be published in the *Proceedings of 1989 Materials Research Society Fall Meeting: Beam-Solid Interactions,* Boston, MA, 27 November–2 December 1989; and in *Physical Review Letters*.

P. C. Cheng, V. H.-K. Chen, H. Kim, and R. E. Pearson, "A Real-Time EPI-Fluorescent Confocal Microscope," to be published in *Journal of Microscopy*.

P. C. Cheng, V. H.-K. Chen, H. Kim, and R. E. Pearson, "An EPI-Fluorescent Spinning-Disk Confocal Microscope," to be published in the *Proceedings of the 47th Annual Meeting of Electron Microscopy Society of America* (EMSA), Austin, TX, 14–18 August 1989.

H. E. Elsayed-Ali and J. W. Herman, "Picosecond Time-Resolved Surface-Lattice Temperature Probe," to be published in *Applied Physics Letters.*

H. E. Elsayed-Ali, T. Juhasz, G. O. Smith, and W. E. Bron, "Femtosecond Thermoreflectivity and Thermotransmissivity of Polycrystalline and Single-Crystalline Gold Films," to be published in *Physical Review B.*

E. M. Epperlein, "Electron Kinetics in Laser-Driven Inertial Confinement Fusion," to be published in the *Proceedings of the Topical Conference on Research Trends in Nonlinear and Relativistic Effects in Plasmas,* La Jolla, CA, 5–8 February 1990.

E. M. Epperlein, "Kinetic Theory of Laser Filamentation in Plasmas," to be published in *Physical Review Letters.*

R. Epstein, "Satellite Absorption Lines and the Temperature Dependence of X-Ray Absorption Features in High-Temperature Plasmas," to be published in *Physical Review A.*

S. D. Jacobs, "Optical Materials: Improved Building Blocks for Better Lasers," to be published in *Chemtech.*

H. Kim, C. K. Immesoete, and S. Scarantino, "Computer-Assisted Microballoon Selection for Inertial Fusion Targets," to be published in the *Proceedings of the Seventh Target Fabrication Specialists Meeting,* Livermore, CA, 25–29 September 1989.

H. Kim, R. Q. Gram, M. D. Wittman, C. Immesoete, R. S. Craxton, N. Sampat, S. Swales, G. Pien, and J. M. Soures, "Uniform Liquid Fuel Layer Produced in a Cryogenic Target by a Time-Dependent Thermal Gradient," to be published in the *Proceedings of the Seventh Target Fabrication Specialists Meeting,* Livermore, CA, 25–29 September 1989.

L. E. Kingsley and W. R. Donaldson, "Electro-Optic Imaging of Surface Electric Fields in High-Power Photoconductive Switches," to be published in *IEEE Transactions on Electron Devices.*

J. C. Lambropoulos and S.-S. Hwang, "Film Thermal Conductivity and Laser Damage Resistance of Optical Thin Films," to be published in the *Proceedings of a Symposium on Electro-Optics and Non-Linear Optics,* 1st International Congress on Ceramic Science and Technology, Anaheim, CA, 1–3 November 1989.

J.-C. Lee and S. D. Jacobs, "Design and Construction of 1064 nm Liquid Crystal Laser Cavity End Mirrors," to be published in *Applied Physics Letters.*

J.-C. Lee, S. D. Jacobs, and K. J. Skerrett, "Laser Beam Apodizer Utilizing Gradient-Index Optical Effects in Liquid Crystals," to be published in *Optical Engineering.*

G. G. Luther, C. J. McKinstrie, and A. L. Gaeta, "The Transverse Modulational Instability of Counterpropagating Light Waves," to be published in the *Proceedings of the Topical Meeting on Nonlinear Dynamics in Optical Systems,* Afton, OK, 4–8 June 1990.

R. L. McCrory, "New Research Trends in Inertial Confinement Fusion," to be published in the *Proceedings of the Topical Conference on Research Trends in Nonlinear and Relativistic Effects in Plasmas,* La Jolla, CA, 5–8 February 1990.

R. L. McCrory and C. P. Verdon, "Computer Modeling and Simulation in Inertial Confinement Fusion," to be published in *Il Nuovo Cimento.*

R. L. McCrory and C. P. Verdon, "Inertial Confinement Fusion: Computer Simulation," to be published as a book chapter in *Computer Applications of Plasma Science and Engineering.*

R. L. McCrory, J. M. Soures, J. Knauer, S. Letzring, F. J. Marshall, S. Skupsky, W. Seka, C. Verdon, D. Bradley, R. S. Craxton, J. Delettrez, R. Epstein, P. Jaanimagi, R. Keck, T. Kessler, H. Kim, R. Kremens, P. W. McKenty, R. Short, and B. Yaakobi, "Direct-Drive Implosion Experiments at the Laboratory for Laser Energetics," to be published in the *Proceedings of the Thirteenth International Conference on Plasma Physics and Controlled Nuclear Fusion Research,* Washington, DC, 1–6 October 1990.

P. W. McKenty, C. P. Verdon, S. Skupsky, R. L. McCrory, D. K. Bradley, W. Seka, and P. A. Jaanimagi, "Numerical Modeling of Effects of Power Imbalance on Irradiation Nonuniformities," to be published in the *Journal of Applied Physics.*

C. J. McKinstrie and R. Bingham, "Stimulated Raman Forward Scattering and the Relativistic Modulational Instability of Light Waves in Rarefied Plasma," to be published in *Physics of Fluids B.*

Conference Presentations

The following presentations were made at the SPIE/1990 International Symposium on Optical and Optoelectron Applied Science and Engineering: Advanced Optical Production Technology, San Diego, CA, 8–13 July 1990:

D. Golini and S. D. Jacobs, "Transition Between Brittle and Ductile Mode in Loose Abrasive Grinding of ULE."

P. A. Jaanimagi and C. Hestdalen, "Streak Camera Phosphors: Response to Ultra-Short Excitation."

The following presentations were made at the 20th Annual Anomalous Absorption Conference, Traverse City, MI, 9–13 July 1990:

T. Boehly, M. Russotto, R. Epstein, R. S. Craxton, B. Yaakobi, B. MacGowan, L. DaSilva, J. Nilsen, E. Chandler, D. Matthews, and M. Eckhart, "Experiments in Photo-Pumped X-Ray Lasers."

D. K. Bradley, J. A. Delettrez, P. A. Jaanimagi, and C. P. Verdon, "The Effect of Smoothing by Spectral Dispersion (SSD) on Burnthrough Measurements Using the OMEGA Laser System."

Y.-H. Chuang and D. D. Meyerhofer, "Suppression of the Pedestal and Pre-Pulse in a Chirped-Pulse-Amplification Laser."

Y.-H. Chuang, H. Chen, S. Uchida, and D. D. Meyerhofer, "Initial Laser-Plasma Formation."

R. S. Craxton, W. Seka, and D. L. Brown, "Optical Probing Diagnostics for the OMEGA Upgrade."

J. Delettrez, H. Chen, E. Epperlein, D. D. Meyerhofer, and S. Uchida, "Effects of Nonlocal Thermal and Suprathermal Electron Transport in Simulations of 1-ps Laser Pulse Interaction."

E. Epperlein, "Kinetic Theory of Laser Beam Thermal Filamentation in Plasmas."

R. Epstein, "Satellite Absorption Lines and the Temperature Dependence of X-Ray Absorption Features in High-Temperature Plasmas."

G. G. Luther, C. J. McKinstrie, and A. L. Gaeta, "Transverse Modulational Instability of Counterpropagating Waves and Conical Radiation."

C. J. McKinstrie, L. Mu, M. Yum, and R. Bingham, "Stimulated Raman Forward Scattering and the Relativistic Modulational Instability of Light Waves in Rarefied Plasma."

D. D. Meyerhofer, D. Bradley, Y.-H. Chuang, H. Chen, J. Delettrez, R. Epstein, P. Jaanimagi, S. Uchida, and B. Yaakobi, "Results from High-Intensity, 1 ps, Laser-Plasma Interaction Experiments."

K. Mizuno, W. Seka, R. Bahr, R. P. Drake, and J. S. DeGroot, "Development of a Collective Thomson Scattering Diagnostic Using the Ion Acoustic Decay Instability."

W. Seka, R. S. Craxton, R. Bahr, D. Bradley, P. Jaanimagi, J. Knauer, S. Letzring, D. Meyerhofer, S. Morse, R. W. Short, A. Simon, C. Verdon, and J. M. Soures, "Long Scale Length Interaction Experiments on OMEGA."

R. W. Short, "Filamentation of Obliquely Incident Laser Light in Inhomogeneous Plasmas."

A. Simon, "Caviton Burnout, the Bump-on-Tail Electron Velocity Distribution, and Fast Ion Beams."

S. Uchida, H. Chen, Y.-H. Chuang, J. Delettrez, and D. D. Meyerhofer, "Hot Electron Energy Transport in Picosecond Laser-Plasma Interactions."

The following presentations were made at the X-Ray Microscopy 1990 Conference, London, England, 3–7 September 1990:

P. C. Cheng and H. Kim, "The Study of Silica Deposition in Maize by X-Ray Microradiography and Confocal Light Microscopy."

H. Kim, B. Yaakobi, J. M. Soures, and P. C. Cheng, "Laser-Produced Plasma as a Light Source for X-ray Microscopy."

J. Delettrez, "Simulation of Short-Pulse Interaction," presented at the 1990 CECAM Workshop, Orsay, France, 10–12 September 1990.

T. Boehly, M. Russotto, B. Yaakobi, R. Epstein, R. S. Craxton, L. DaSilva, J. Nilsen, B. MacGowan, G. Shimkaveg, A. R. Fry, E. Chandler, D. Matthews, and M. Eckart, "Demonstration of a Resonantly Photo-Pumped X-Ray Laser," presented at the 2nd International Colloquium on X-Ray Lasers, York, England, 17–21 September 1990.

P. A. Jaanimagi, C. Hestdalen, J. Kelly, and W. Seka, "High Precision Measurements of the 24-Beam UV OMEGA Laser," presented at the 19th International SPIE Congress on High-Speed Photography and Photonics, Cambridge, England, 17–21 September 1990.

D. D. Meyerhofer, S. Augst, C. Moore, J. Peatross, J. H. Eberly, and S. L. Chin, "Barrier Suppression Ionization and High-Order Harmonic Generation in Noble Gases at Laser Intensities of 1 Atomic Unit and Above," presented at the International Conference on Multiphoton Processes (ICOMP V), Paris, France, 24–28 September 1990.

ACKNOWLEDGMENT

The work described in this volume includes current research at the Laboratory for Laser Energetics, which is supported by Empire State Electric Energy Research Corporation, New York State Energy Research and Development Authority, Ontario Hydro, the University of Rochester, and the U.S. Department of Energy Division of Inertial Fusion under agreement No. DE-FC03-85DP40200.